JGR Solid Earth

RESEARCH ARTICLE
10.1029/2021JB023410

Preventing Instabilities and Inducing Controlled, Slow-Slip in Frictionally Unstable Systems

Ioannis Stefanou[1] and **Georgios Tzortzopoulos**[1]

[1]Ecole Centrale de Nantes, Université de Nantes, CNRS GeM (Institut de Recherche en Génie Civil et Mécanique), Nantes, France

Key Points:

- We present a theory for preventing dynamic events, inducing slow-slip and allowing smooth energy release in frictionally unstable systems
- We use the mathematical theory of control and we derive robust controllers covering a wide range of uncertainties and unmodeled dynamics
- We provide numerical examples of robust control for Generalized Burridge-Knopoff systems and seismic fault models

Supporting Information:

Supporting Information may be found in the online version of this article.

Correspondence to:

I. Stefanou,
ioannis.stefanou@ec-nantes.fr

Citation:

Stefanou, I., & Tzortzopoulos, G. (2022). Preventing instabilities and inducing controlled, slow-slip in frictionally unstable systems. *Journal of Geophysical Research: Solid Earth*, *127*, e2021JB023410. https://doi.org/10.1029/2021JB023410

Received 16 OCT 2021
Accepted 20 MAY 2022

Author Contributions:

Conceptualization: Ioannis Stefanou
Formal analysis: Ioannis Stefanou, Georgios Tzortzopoulos
Funding acquisition: Ioannis Stefanou
Investigation: Ioannis Stefanou, Georgios Tzortzopoulos
Methodology: Ioannis Stefanou
Project Administration: Ioannis Stefanou
Resources: Ioannis Stefanou
Software: Ioannis Stefanou, Georgios Tzortzopoulos

Abstract We propose a theory for preventing instabilities and inducing controlled, slow-slip in frictionally unstable systems, such as the Generalized-Burridge-Knopoff (GBK) model and seismic fault models. We exploit the dependence of friction on pressure and use it as a backdoor for altering the dynamics of the underlying dynamical system. We use the mathematical Theory of Control and, for the first time, we manage to (a) stabilize and restrict chaos in this kind of systems, (b) guarantee slow frictional dissipation and (c) tune the system toward desirable global asymptotic equilibria of lower energy. Our control approach is robust and does not require exact knowledge of the frictional or elastic behavior of the system. Numerical examples of control are given for a Burridge-Knopoff system and a strike-slip fault model obeying rate-and-state friction. GBK models are known to present Self-Organized Critical (SOC) behavior. Therefore, the presented methodology shows an additional example of SOC Control. Even though further developments are necessary before any practical application, we expect our methodology to inspire earthquake mitigation strategies regarding anthropogenic and/or natural seismicity.

Plain Language Summary Frictional instabilities are omnipresent in nature. A characteristic example is that of earthquakes. Earthquakes are dynamic instabilities that occur when the elastic unloading of the rocks surrounding a fault zone cannot be counterbalanced by fault friction. Recent experience shows that friction can be altered by injecting fluids in the earth's crust. However, until now, most attempts of fluid injections result, sooner or later, in provoking earthquakes. In this work, we present a general mathematical theory that shows that it is possible to adjust the fluid pressure to prevent these instabilities. Moreover, we show how we can induce slow-slip and allow smooth energy relaxation in such systems. We show also how to drive these systems to desirable stable equilibria of lower energy in a controlled manner. This is achieved even in the absence of complete information about the frictional properties and other uncertainties and unmodeled dynamics. In order to illustrate the theory, we provide numerical examples for spring-dashpot-slider (Burridge-Knopoff) systems, which are characterized by rich dynamics, chaos and self-organized criticality, and for a seismic fault model. The current limitations of the proposed approach are also extensively discussed. The proposed theoretical framework could inspire strategies for controlling anthropogenic and natural seismicity.

1. Introduction

The main objective of this work is to show how the chaotic, rich dynamics of frictionally unstable systems can be altered and controlled. We mainly focus on Generalized Burridge-Knopoff (GBK) models and seismic fault models, and we show how slow-slip and smooth energy relaxation can be achieved in a controlled and designed manner.

Our control theory is inspired by the recent experience that humans *do cause* earthquakes by injecting fluids in the earth's crust, which potentially lead to fault reactivation and induced/triggered seismicity (Cappa et al., 2019; Cornet, 2016; Guglielmi et al., 2015; Keranen et al., 2013; McGarr et al., 2002; Raleigh et al., 1976; Rubinstein & Mahani, 2015). These unwanted seismic events can have important consequences for active industrial projects (see for instance conventional and unconventional energy production in oil and gas industry, renewable energies like deep geothermal projects and CO_2 sequestration).

In this work, the problem of fluid injections is seen from another perspective. We exploit the dependence of friction on fluid pressure and we use it as backdoor for altering the dynamics of an underlying chaotic system.

Supervision: Ioannis Stefanou
Validation: Ioannis Stefanou, Georgios Tzortzopoulos
Visualization: Georgios Tzortzopoulos
Writing – original draft: Ioannis Stefanou
Writing – review & editing: Ioannis Stefanou, Georgios Tzortzopoulos

The main ingredient of our approach is the *modern mathematical Theory of Control* (Khalil, 2015; Vardulakis, 1991, 2012), which is applied in order to:

1. Stabilize the unstable frictional system;
2. Drive it quasi-statically to lower energy levels and stable equilibria.

This is achieved without precise knowledge of the mechanical parameters of the system and of its heterogeneous and uncertain frictional and elastic properties. A key element of this work is the mathematical proof that control is possible provided that the friction coefficient is *Lipschitz continuous* (Abbott, 2015; Brauer & Nohel, 1969) with respect to the states of the system. In other words, the rate of change of the friction coefficient with respect to the slip and/or the slip-rate should be finite (limited/bounded). Lipschitz continuity is a reasonable assumption for friction, given that any unmodeled and unknown physical process will have finite influence on the friction coefficient, due to its own finite spatio-temporal scales and finite energy.

The mathematical developments presented herein are kept as general as possible. The developed controller is designed for tackling a general class of non-linear ordinary differential equations systems, which involve friction, independently of the frictional rheology (e.g., slip-weakening, slip-rate weakening (SRW), rate-and-state friction (RSF), or other rheologies involving multiphysics couplings). This allows us to cover a variety of physical situations involving frictionally unstable systems.

Our theory is first applied to control the rich and chaotic dynamics of Generalized Burridge-Knopoff (GBK) models (see Burridge & Knopoff, 1967; Huang et al., 1992; Ito & Matsuzaki, 1990, among others). Burridge-Knopoff models consist of several interconnected elements (masses) that can slide on a rough surface under friction. The sliding masses are connected to a driver plate that slowly transfers load and energy to the system. For more details about this model we refer to Section 3. This kind of systems are characterized by slow and fast dynamics and show spatio-temporal correlations due to the interconnectivity of their elements. The continuous slow movement of the driver plate leads to instabilities expressed as abrupt sliding of clusters of elements. GBK show rich dynamic behavior, chaos and manifest self-organized criticality. Notice that due to the absence of long-range interactions among (very) distant elements, Burridge-Knopoff models may exhibit more instabilities than seismic fault models. As such, they become a very interesting benchmark for showing the capabilities of our theory.

Next, we proceed by applying our control theory to seismic fault models. Our control theory can be applied directly in any fault configuration, provided that a consistent spatial discretization of the continuum elastodynamic boundary value problem is given (e.g., with the Finite Element Method, Finite Differences, Boundary Elements, spectral methods, among others (Boyd, 2000)). Here we present an example of a strike-slip fault, which obeys RSF (Dieterich, 1979). In our simulations, the RSF parameters are heterogenous over the fault area and they follow a log-normal distribution. We show how the proposed theory can drive aseismically the system to a new stable state, without even knowing the exact friction law that characterizes fault slip.

Inevitably, our theoretical framework could be used for exploring new strategies for earthquake control. Controlling earthquakes is not a new idea. In the 70s, Raleigh et al. (1976) have shown how fluid injections could enhance or mitigate seismicity at the Rangely Oil Field in Colorado, USA. Despite their encouraging results, the authors raised concern about the feasibility of controlling the behavior of faults due to many hypothetical factors that could preclude the possibility of obtaining any degree of useful control. These hypothetical factors refer mainly to the uncertainties related to the physical properties of the geosystem, the available data and cost. However, the recent human activity, related to energy production, revived the need for fault stabilization and seismic risk reduction. Numerous laboratory and field experiments focused on determining factors influencing the transition from seismic to a-seismic slip during fluid injections (see Cappa et al., 2019; Guglielmi et al., 2015; Scuderi & Collettini, 2018; Tinti et al., 2016; Tzortzopoulos et al., 2021, among others). Seismic traffic-light systems have been also proposed for minimizing seismicity and risks to acceptable levels (see Baisch et al., 2019; Bommer et al., 2006; Bommer et al., 2015; Bosman et al., 2016; Broccardo et al., 2020; Häring et al., 2008; Kwiatek et al., 2019; Verdon & Bommer, 2021; Walters et al., 2015). More recently, "cyclic stimulation" (Hofmann et al., 2018, 2019; Zang et al., 2019) and "fracture caging" (Frash et al., 2021) were proposed for limiting induced seismic events in geothermal energy projects. In the former, fluids are injected in a reservoir with cyclically varying injection rates. In the latter, wells are drilled in order to encage (contain) high-pressure fluids from injection wells within a targeted volume.

Despite the plethora of the proposed strategies and variations, the concerns raised by Raleigh et al. (1976) remain still valid and none of them can provide a rigorous mathematical framework where the question of earthquake control could be explored in a systematic and effective way. We believe that the proposed approach is a first step toward this direction.

The paper is organized as follows. In Section 2, we present the theoretical developments for control. The mathematical proofs for stabilization and asymptotic tracking are given in details in this Section. Requirement for our control method to be effective is the boundedness of the rate of change of friction with respect to slip and/or slip-rate. Therefore, we proceed with deriving bounds of common frictional laws, such as the slip and SRW frictional laws and the RSF model. The influence of multiphysics couplings on friction and their boundedness is discussed as well. In Section 3, we provide the main ingredients of the Generalized Burridge-Knopoff formulation used here and we confirm its well-known *Self-Organized Critical* (SOC) behavior by the means of a numerical example. Then, we show how the input pressure can be adjusted in real-time for assuring slow-slip and driving the system to lower (potential) energy states (robust tracking). In Section 4, we apply the developed theory for controlling seismic slip over a strike-slip fault under RSF. The results of our approach are discussed extensively in the last Section of this work, where perspectives, limitations and implications of the current framework are given for SOC Control (SOCC) and geophysics, in general, and for man-made and natural earthquakes, in particular.

2. Theory

The class of nonlinear systems that are studied herein are represented by the following non-linear system of differential equations:

$$x' = A(x,t)x + B(x,t)u + g(x,t), \tag{1a}$$

$$y = C_o x, \tag{1b}$$

where $t \geq 0$ is the time, $x = x(t) \in \mathbb{R}^n$ the state vector, $x' = \frac{dx}{dt} \in \mathbb{R}^n$ the time derivative of the state vector, $u \in \mathbb{R}^p$ the input vector, $y \in \mathbb{R}^m$ the output vector, $A \in \mathbb{R}^{n\times n}$, $B \in \mathbb{R}^{n\times p}$, $C_o \in \mathbb{R}^{m\times n}$, and $g \in \mathbb{R}^n$ matrices and vector, respectively, with potential nonlinear elements. We assume that the above system is shifted in such a way that the origin ($x = 0$) is an equilibrium, that is, $x' = 0$.

The vector $g(x,t)$ contains the frictional terms of the system. The matrix $A(x,t)$ represents elastic, viscoelastic or inelastic phenomena (see Fung, 1965) of the rock surrounding the fault zone. Its exact components are determined by spatially discretizing the differential operators that correspond to (visco-)elastic and inertia effects on the basis of appropriate discretization methods. The matrix $B(x,t)$ contains the influence of injected fluid pressure changes (input u) to the dynamics of the system through friction. Both matrices $A(x,t)$ and $B(x,t)$ can contain uncertainties and unmodeled dynamics. Therefore, we decompose them into a nominal (known) and perturbed/deviated (unknown/uncertain) part:

$$A(x,t) = A_0 + \Delta A(x,t), \tag{2a}$$

$$B(x,t) = B_0 + \Delta B(x,t), \tag{2b}$$

where A_0 and B_0 are chosen to be constant matrices, such that the pair (A_0, B_0) to be stabilizable. ΔA and ΔB are perturbations from the nominal system. This additive decomposition is always possible for the applications presented in this work.

Inserting Equations (2) into Equation (1a), we obtain:

$$x' = A_0 x + B_0 u + \Delta B(x,t)u + f(x,t), \tag{3}$$

where $f(x,t) = \Delta A(x,t)x + g(x,t)$. Assuming matched uncertainties (Khalil, 2015), the vector f can be rewritten as $f(x,t) = B_0 B_0^+ f(x,t)$, where $B_0^+ \in \mathbb{R}^{p\times n}$ is the *Moore-Penrose inverse matrix* of B_0. After rearrangement of some terms, Equation (3) yields:

$$x' = A_0 x + \Delta B(x,t)u + B_0 \left(u + h(x,t)\right), \tag{4}$$

where $h(x,t) = B_0^+ f(x,t)$ is assumed to be *Lipschitz continuous* (Abbott, 2015; Brauer & Nohel, 1969):

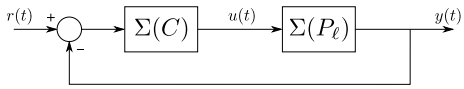

Figure 1. Negative feedback control system $\Sigma(P_\ell, C)$. $\Sigma(P_\ell)$ is the Generalized Burridge-Knopoff or the seismic fault system (plant) to be controlled (Equation (1)) using the proposed robust controller $\Sigma(C)$ (see Sections 2.1 and 2.2).

$$\|h(x,t)\| \leq \beta\|x\|, \tag{5}$$

with $\beta > 0$, and $\|\cdot\|$ being the Euclidean norm. Therefore, if friction is a Lipschitz function (see Section 2.3) and ΔA bounded, then $h(x,t)$ is also Lipschitz.

The dynamics of the above system will be controlled using the mathematical theory of control (Khalil, 2015; Vardulakis, 1991, 2012). The target is to update the input, u, which in the applications presented in Sections 3 and 4 corresponds to the pressure of fluids injected (added) and pumped (removed) at the frictional interfaces, in order to stabilize it, that is, to avoid abrupt, seismic slip and sudden energy release. The term stability is used here in the Lyapunov sense (that is, the system remains close to its equilibrium state under small perturbations from it; for a rigorous mathematical definition of Lyapunov stability we refer to Lyapunov (1966) and Stefanou and Alevizos (2016)).

We consider a general *negative feedback* control system as depicted in Figure 1. $\Sigma(P_\ell)$ is the multivariable system (plant) to be controlled described by Equation (1), and $\Sigma(C)$ is the stabilizing controller we need to design. $y(t)$ is the output of the closed-loop, controlled system $\Sigma(P_\ell, C)$ and $u(t)$ the input of the plant. $r(t)$ is a desired state of the system, such that $\lim_{t\to\infty} y = r$. First, we seek the controller $\Sigma(C)$ that can immobilize (or stabilize at the origin in terms of Lyapunov stability) the system ($r(t) = 0$). Then, we will consider specific forms for r (e.g., constant, non null velocity) in order to drive the system smoothly to a desired stable equilibrium point and dissipate the energy in a controlled manner. In the frame of the mathematical theory of control, this process is called *tracking*.

In Sections 2.1 and 2.2, we provide the necessary mathematical proofs and we derive the controllers that will allow us to stabilize and control the unstable seismic slip by adjusting the fluid pressure on the frictional interfaces. The approach is based on the second method of Lyapunov for proving stability (Brauer & Nohel, 1969; Khalil, 2015). Notice that these mathematical proofs are central and support the conclusions drawn in this work. The numerical simulations that follow in Sections 3 and 4 illustrate the consequences of these mathematical derivations.

2.1. Robust State Feedback Stabilization

Let the scalar function $V(x) = x^{\mathrm{T}}\Theta x > 0$ for all non-zero $x \in \mathbb{X} \subset \mathbb{R}^n$ and $V(0) = 0$. Under these conditions, $\Theta \in \mathbb{R}^{n\times n}$ is called *positive definite*, that is, $\Theta \succ 0$ (or *negative definite* if $x^{\mathrm{T}}\Theta x < 0\ \forall x \in \mathbb{X} \subset \mathbb{R}^n \backslash 0$, i.e., $\Theta \prec 0$).

We will design a constant negative full-state feedback ($C_o = I_n$) robust controller of the form $u = -Kx = -R^{-1}B_0^{\mathrm{T}}\Theta x$,where $K \in \mathbb{R}^{p\times n}$ is the gain matrix and $R \in \mathbb{R}^{p\times p}$ is selected to be positive definite.

According to Lyapunov's stability theorem (see *Lyapunov's Second Method,* Brauer & Nohel, 1969), if there exists $V(x) > 0$ for which $\frac{dV(x)}{dt} = V'(x)$ is strictly negative $\forall x \in \mathbb{X} \subset \mathbb{R}^n \backslash 0$, then the origin of the system, $x = 0$, is asymptotically stable. If $\mathbb{X}$ extends over the whole real n-dimensional Euclidean space, then the origin is *globally* asymptotically stable. Differentiating $V(x)$ with respect to time we obtain:

$$V' = x'^{\mathrm{T}}\Theta x + x^{\mathrm{T}}\Theta x' \tag{6a}$$

$$= x^{\mathrm{T}}\left(A_0^{\mathrm{T}}\Theta + \Theta A_0 - \Theta B_0 R^{-1} B_0^{\mathrm{T}}\Theta\right)x - x^{\mathrm{T}}\Theta B_0 R^{-1} B_0^{\mathrm{T}}\Theta x - \\ -2x^{\mathrm{T}}\Theta\frac{B_0 R^{-1}\Delta B^{\mathrm{T}} + \left(B_0 R^{-1}\Delta B^{\mathrm{T}}\right)^{\mathrm{T}}}{2}\Theta x + 2x^{\mathrm{T}}\Theta B_0 h. \tag{6b}$$

The first term of the right hand side of Equation (6b) is part of a Continuous Algebraic Riccati Equation (see also Zhou et al., 1996) of the form:

$$A_0^{\mathrm{T}}\Theta + \Theta A_0 - \Theta B_0 R^{-1} B_0^{\mathrm{T}}\Theta = -Q \tag{7}$$

that can be solved numerically (see Appendix C). $Q \in \mathbb{R}^{n\times n}$ is positive definite. Equation (7) has a unique positive definite solution $\Theta \succ 0$ if the pair (A_0, B_0) is stabilizable, Q is (at least) *positive semi-definite* (i.e., $Q \succeq 0$ if $x^{\mathrm{T}}Qx \geq 0\ \forall x \in \mathbb{X} \subset \mathbb{R}^n \backslash 0$) and $R \succ 0$. Moreover, should we design the nominal matrix B_0 such that the

non-Hermitian matrix $B_0 R^{-1} \Delta B^{\mathrm{T}}$ to be always positive semi-definite, the third term of the right-hand side of Equation (6b) is a non-positive number. Setting $z = R^{-1/2} B_0^{\mathrm{T}} \Theta x$, Equation (6) becomes:

$$V' \leq -x^{\mathrm{T}} Q x - z^{\mathrm{T}} z + 2 z^{\mathrm{T}} R^{1/2} h, \tag{8}$$

where $R^{-1} = R^{-1/2} R^{-1/2}$. We choose the positive semi-definite matrix Q in such a way that Equation (8) to be strictly negative for any given pair of (t, x). Such a design should contain the uncertainties and non-linearities embedded in vector h (see Equation (5)). Let:

$$Q = Q_0 + \beta^2 \| R^{1/2} \|^2 I_n, \tag{9}$$

where $Q_0 \succ 0$ is to be specified depending on the application and I_n is the identity matrix of size n. Substituting Equation (9) to Equation (8) yields:

$$V' \leq -x^{\mathrm{T}} Q_0 x - \beta^2 \| R^{1/2} \|^2 x^{\mathrm{T}} x - z^{\mathrm{T}} z + 2 z^{\mathrm{T}} R^{1/2} h \tag{10a}$$

$$\leq -x^{\mathrm{T}} Q_0 x - \beta^2 \| R^{1/2} \|^2 \|x\|^2 - \|z\|^2 + 2\beta \| R^{1/2} \| \|z\| \|x\| \tag{10b}$$

$$\leq -x^{\mathrm{T}} Q_0 x - \underbrace{\left(\beta \| R^{1/2} \| \|x\| - \|z\| \right)^2}_{\geq 0} \tag{10c}$$

$$\leq -\underbrace{x^{\mathrm{T}} Q_0 x}_{>0} < 0. \tag{10d}$$

The above inequality is valid for any $x \in \mathbb{R}^n$. Therefore, the closed-loop system of Figure 1 ($\Sigma(P_\ell, C)$) is globally exponentially stable (Khalil, 2015). Consequently, independently of the initial conditions, $\lim_{t \to \infty} x(t) = 0$.

Summarizing, for the design of the controller, the matrices A_0, B_0, Q_0, and R as well as the β coefficient are problem dependent and have to be determined as explained above.

2.2. Robust Tracking

Let $r(t) \in \mathbb{R}^q$ denote the reference input signals that we want to track, with $q \leq p$ (see Lewis et al., 2012). For this purpose, we apply the method of *integral action* (Khalil, 2015). Assuming that the dynamics of the designed controller are well represented by q single integrators and that the reference input vector $r(t)$ is a step command with magnitude r_0, the compensator dynamics can be expressed by the following set of equations:

$$\xi' = e = C_t x - r_0, \tag{11a}$$

$$w = \xi, \tag{11b}$$

where $\xi \in \mathbb{R}^q$ expresses the integral of the error, $e \in \mathbb{R}^q$, between the actual and the desired state, r_0. The multiplication with the matrix $C_t \in \mathbb{R}^{q \times n}$ expresses a linear combination of the outputs of the system in which we want to apply tracking (Equation (1)) and $w \in \mathbb{R}^q$ is the controller's output vector for tracking.

By augmenting the system of Equations (1) with Equations (11), we get:

$$\underbrace{\begin{bmatrix} x' \\ \xi' \end{bmatrix}}_{x_a'} = \underbrace{\begin{bmatrix} A & O_{n \times q} \\ C_t & O_{q \times q} \end{bmatrix}}_{A_a} \underbrace{\begin{bmatrix} x \\ \xi \end{bmatrix}}_{x_a} + \underbrace{\begin{bmatrix} B \\ O_{q \times m} \end{bmatrix}}_{B_a} \underbrace{\begin{bmatrix} u \end{bmatrix}}_{u_a} + \underbrace{\begin{bmatrix} O_{n \times q} \\ -I_q \end{bmatrix}}_{R_a} \begin{bmatrix} r_0 \end{bmatrix} + \underbrace{\begin{bmatrix} g \\ O_{q \times 1} \end{bmatrix}}_{g_a}, \tag{12a}$$

$$\underbrace{\begin{bmatrix} y \\ w \end{bmatrix}}_{y_a} = \underbrace{\begin{bmatrix} C_o & O_{m \times q} \\ O_{q \times n} & I_q \end{bmatrix}}_{C_a} \underbrace{\begin{bmatrix} x \\ \xi \end{bmatrix}}_{x_a}, \tag{12b}$$

where $O_{i\times j}$ denotes the zero matrix with i rows and j columns. In compact form, the above equations are written as follows:

$$x'_a = A_a x_a + B_a u_a + R_a r_0 + g_a, \tag{13a}$$

$$y_a = C_a x_a. \tag{13b}$$

Considering again full-state feedback ($C_a = I_{n+q}$), the input vector u_a is of the form:

$$u_a = -K_a x_a. \tag{14}$$

at steady-state Equations (13) yield:

$$0 = A_a x_a^{eq} + B_a u_a^{eq} + R_a r_0 + g_a^{eq}, \tag{15a}$$

$$y_a^{eq} = C_a x_a^{eq}. \tag{15b}$$

By applying the transformation $\tilde{x}_a(t) = x_a(t) - x_a^{eq}$, $\tilde{y}_a(t) = y_a(t) - y_a^{eq}$, $\tilde{u}_a(t) = u_a(t) - u_a^{eq}$, $\tilde{g}_a(t) = g_a(t) - g_a^{eq}$, Equations (13) become:

$$\tilde{x}'_a = A_a \tilde{x}_a + B_a \tilde{u}_a + \tilde{g}_a, \tag{16a}$$

$$\tilde{y}_a = C_a \tilde{x}_a. \tag{16b}$$

Using the same transformation, Equation (14) becomes:

$$\tilde{u}_a = -K_a \tilde{x}_a. \tag{17}$$

The above system of equations is of the form of Equations (1) for which a robust stabilizing controller was derived in the previous paragraph. Consequently, if the input respects Equation (17) or, equivalently, Equation (14), then $\lim_{t\to\infty} e(t) = 0$ or $\lim_{t\to\infty} C_t x = r_0$ and so the reference input step command, r_0, is tracked robustly. For time varying reference trajectories, $r(t)$, we expect a steady state error, which can be eliminated by adding more integrators (that is., q double integrators, see Tzortzopoulos, 2021a; Gutiérrez-Oribio et al., 2022) or reduced by increasing the relevant integral action gains.

2.3. Boundedness of Friction

Friction between materials in contact is a complex phenomenon and involves dissipative phenomena at different length and time scales. Moreover, friction depends on the fabric, the deformation history and the heterogeneities of the materials in contact. Consequently, friction is, in general, hard to quantify in practice without large uncertainties.

In the frame of fault mechanics, the most common frictional models that can lead to earthquake-like instabilities are the Slip Weakening, SRW and RSF laws (see Byerlee, 1978; Dieterich, 1981; Kanamori & Brodsky, 2004; Scholz, 2019, among others). More advanced constitutive models have been also proposed in the literature. These physics-based models can take into account, in a direct manner, various Thermo-Hydro-Chemo-Mechanical phenomena that arise during frictional sliding (see Barras et al., 2019; Bhattacharya & Viesca, 2019; Chester, 1994; Collins-Craft et al., 2020; Kenigsberg et al., 2020; Lachenbruch, 1980; Rattez & Veveakis, 2020; Rattez, Stefanou, & Sulem, 2018; Rattez, Stefanou, Sulem, Veveakis, & Poulet, 2018; Rudnicki & Chen, 1988; Stathas & Stefanou, 2022; Vardoulakis, 2000, and references therein, among others). Nevertheless, despite the rich literature on that topic, the quantification of the frictional properties is not a trivial task and it would always lead to estimations characterized by uncertainties (cf. Rice, 2006).

However, this does not mean that these uncertainties are unbounded. In the following paragraphs, we show that the aforementioned popular frictional models are Lipschitz continuous functions (bounded rate of change with respect to slip and/or slip-rate). Consequently, our control approach is applicable even without precise knowledge of the exact frictional parameters and their spatial distribution. Moreover, our approach can cover unmodeled dynamics influencing friction, provided that the Lipschitz condition is satisfied as shown below.

2.3.1. Slip-Weakening Friction

In the slip-weakening friction law, the coefficient of friction, μ, evolves from an initial value μ_s (static friction coefficient), to a residual one μ_d (kinetic friction coefficient). This transition is made in a characteristic slip distance d_c (Kanamori & Brodsky, 2004). The slip-weakening law is often expressed through the following exponential decay function, whose parameters can be calibrated based on experimental data:

$$\mu = \mu(\delta) = \mu_d + \Delta\mu e^{-\frac{\delta}{d_c}}, \tag{18}$$

where $\delta > 0$ is the slip and $\Delta\mu = \mu_s - \mu_d > 0$. Exploiting the properties of the exponential function, we can show that there exists $\gamma \geq \frac{\Delta\mu}{d_c} > 0$ such that $|\mu(\delta) - \mu(0)| \leq \gamma|\delta|$. In other words, the rate of change of this slip-weakening friction law with respect to the slip is finite with a determined bound. The same holds for the piece-wise linear slip-weakening law, which also satisfies the above bound.

2.3.2. Slip-Rate Weakening Friction

Another law, that is frequently met in the literature, is the SRW friction law, in which the friction coefficient is expressed in terms of the slip-rate $v > 0$, that is, $\mu = \mu(v)$. An example of such a law is given in Huang and Turcotte (1992) and takes the form:

$$\mu = \mu(v) = \frac{\mu_s}{1 + \frac{v}{v_c}}, \tag{19}$$

where v_c is a characteristic velocity describing the friction coefficient drop due to SRW. Again, it can be shown that there exists $\gamma \geq \frac{\mu_s}{v_c} > 0$ such that $|\mu(v) - \mu(0)| \leq \gamma|v|$. In other words, the rate of change of this SRW friction law with respect to the slip-rate is finite with a determined bound.

2.3.3. Rate-And-State Friction

The most popular friction law that is used for applications in fault mechanics is the RSF law (Dieterich, 1979; Ruina, 1983). According to this model, friction depends logarithmically on the slip-rate and on a state variable that reflects microscopic processes related to contact asperities, healing and creep. This state variable is not to be confused with the state of the dynamical system under study as defined in Equation (1).

Despite the success of this empirical constitutive law to represent experimental data, it does not have a sound thermodynamical basis allowing for a proper balance of energies through external powers and dissipation (Pipping, 2019). This mathematical drawback can be alleviated by proper regularization. Pipping (2019) adopted two possible regularizations that, in the frame of the aging law for the state evolution, can lead to a well defined boundary value problem with unique solution in space and time. According to this author, the friction coefficient can be given using any of the two following expressions:

$$\mu = \mu_r(v, \psi) = a \sinh\frac{v}{2v_\psi} \tag{20}$$

or

$$\mu = \mu_l(v, \psi) = a \ln^+\frac{v}{v_\psi}. \tag{21}$$

in the above expressions, a is a positive coefficient depending on the material, $\ln^+ x = \ln(\max(1, x))$ and:

$$v_\psi = v_0 e^{-\frac{\mu_0 + b\psi}{a}}, \tag{22}$$

where b is a positive coefficient depending on the material and μ_0 and v_0 are reference values for the friction coefficient and the slip velocity, respectively (also dependent on the material). It can be shown that (Pipping, 2019):

$$|\mu_r(v, \psi_2) - \mu_r(v, \psi_1)| \leq |\mu_l(v, \psi_2) - \mu_l(v, \psi_1)| \leq a|\ln\frac{v_{\psi_2}}{v_{\psi_1}}| = b|\psi_2 - \psi_1|, \tag{23}$$

where we set $\psi_1 = \psi(t_1)$, $\psi_2 = \psi(t_2)$, with $t_2 > t_1$. The state variable, ψ, satisfies the general evolution law:

$$\psi' + \lambda(\psi) = f(v), \tag{24}$$

where $\lambda(\psi)$ is a non-decreasing function and $f(v)$ is Lipschitz. In the special case of the aging law, $\lambda(\psi) = -\frac{v_0}{d_c}e^{-\psi}$ and $f(v) = -\frac{v}{d_c}$, with d_c being a characteristic slip distance (Scholz, 2019). By integrating with respect to time Equation (24) and using the non-decreasing property of $\lambda(\psi)$, we obtain $\psi_2 - \psi_1 \leq \int_{t_1}^{t_2} f(v)dt$.

In the case of the aging law, it holds:

$$|\psi_2 - \psi_1| \leq \frac{b}{d_c}|\delta(t_2) - \delta(t_1)|. \tag{25}$$

Using Equations (23) and (25) we can finally show that there exist $\gamma_1 \geq \frac{b}{d_c} > 0$ and $\gamma_2 \geq a > 0$, such that $|\mu(v,\psi) - \mu(0,0)| \leq \gamma_1|\delta| + \gamma_2|v|$. It is worth noticing, that this bound is a combination of the bounds for slip and SRW friction. Therefore, the rate of change of the RSF law with respect to the slip and the slip-rate is finite with a determined bound.

2.3.4. Multiphysics Couplings and Friction

Due to the various complex phenomena that take place in nature, frictional weakening may depend also on temperature, T, fluid pressure, P, chemical reactions, χ, and other multiphysics phenomena. The evolution of these phenomena may depend directly or indirectly on the slip, δ, the slip-rate, v, and on time. We consider these phenomena as unmodeled and uncertain dynamics and we assume them to satisfy the following bound:

$$|\mu(\delta, v, T, P, \chi, \dots, t) - \mu^*| \leq \gamma_1|\delta| + \gamma_2|v| \tag{26}$$

with $\gamma_1 > 0$, $\gamma_2 > 0$ and μ^* being a reference friction coefficient. The explicit dependence of the friction coefficient on time, t, represents unmodeled and uncertain physical processes that can influence friction.

The above inequality signifies that the friction coefficient is a Lipschitz continuous function in terms of slip and slip-rate. Lipschitz continuity is a reasonable assumption given the finiteness in energy of any physical process that can influence the evolution of the friction coefficient. Moreover, the developed slip, slip-rate and the total time of the control operation are design parameters. Therefore, the evolution of several multiphysics phenomena could be roughly estimated in specific situations and conservative bounds for the coefficients γ_1 and γ_2 could be, in principle, estimated and set for achieving control.

3. Control of Generalized Burridge-Knopoff Models

3.1. Equations of Motion

We consider an ensemble of n_b elements of mass m_i each one ($i = 1, 2, .., n_b$), connected through springs and dampers. Each element can slide independently on a rough, horizontal plane as shown in Figure 2. The blocks are connected together and with a plate through springs and dampers. The plate, which is called here *driver plate*, is translated under constant velocity and provides energy to the system, which is progressively stored in the elastic springs. During this phase the system is in stable equilibrium and its total potential energy increases. Due to frictional weakening, at a certain point, this equilibrium becomes unstable and some blocks slide abruptly. During this phase, a part of the stored energy is dissipated abruptly due to friction and damping. The dynamics of this system are described by the following set of non-dimensional equations (for derivation see Appendix A):

$$x' = Ax + h(x), \tag{27}$$

where $x \in \mathbb{R}^{2n_b}$ is the state vector, whose first n_b components represent the dimensionless displacements, $\hat{\delta}_i$, and the rest n_b components the dimensionless velocities, $\hat{v}_i$, of the masses ($i = 1, 2, .., n_b$). $(.)'$ denotes the dimensionless time derivative, the vector $h(x)$ represents the dimensionless forces applied to the blocks due to the initial dimensionless deformation of the springs, $\hat{\delta}_i^0$, the dimensionless displacement, $\hat{\delta}_\infty$, and dimensionless velocity, $\hat{v}_\infty$, of the driver plate, and the dimensionless friction, $\hat{F}_i^r$. It is worth emphasizing that x describes the state of the dynamical system under study and it does not include the so-called state variable in the case of the rate and state friction law (see also Section 2.3.3).

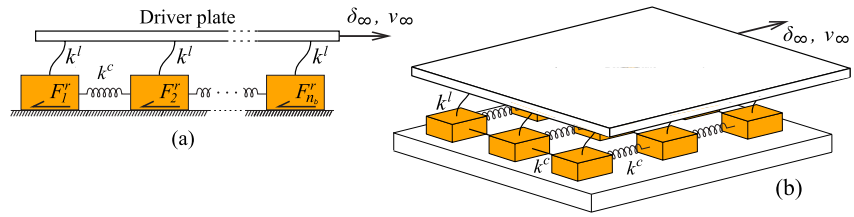

Figure 2. Schematic representation of (a) the Burridge-Knopoff model and (b) its two-dimensional generalization. The dashpots considered in the mathematical model of the current Generalized-Burridge-Knopoff model are not drawn for the sake of simplicity.

The matrix A contains information on how the blocks are connected together and can describe different physical situations. These physical situations cover the classical Burridge-Knopoff model (see Figure 2a and Burridge & Knopoff, 1967; Dieterich, 1972; Carlson & Langer, 1989, among others), its 2D generalization (see Figures 2b and Ito & Matsuzaki, 1990; Brown et al., 1991; Huang et al., 1992, among others) and any other configuration involving short- and long-range interactions of the elements (matrix A can be banded or full). All the physical quantities of the system were scaled as described in Appendix A, where more details are also given about the derivation of the equations of motion.

In the following examples, we assume Coulomb friction, $\hat{F}_i^r = \mu_i \hat{F}_i^n$, where $\hat{F}_i^n$ is the dimensionless effective normal force applied on block i, where $i = 1, 2, .., n_b$, and μ_i is the friction coefficient that, in general, may depend on slip, slip-rate, time and other internal/state variables as discussed in Section 2.3 (without loss of generality zero cohesion is assumed). In the examples presented in this Section, we adopt a slip-weakening friction law (see Section 2.3.1). Key element for the control and arrest of instabilities is the adjustment of the non-dimensional effective normal force $\hat{F}_i^n$. Adjustment of the effective normal force can occur by injecting fluids into the frictional interfaces. Indeed, adopting Terzaghi's principle of effective stress (Terzaghi, 1925), $\hat{F}_i^n = \hat{F}_i^0 - \hat{P}_i$, where $\hat{P}_i$ is the dimensionless resultant force corresponding to the interstitial fluid pressure change at the interface of block i and $\hat{F}_i^0$ is a constant, reference dimensionless normal force (e.g., the weight of the block minus the initial fluid pressure), the dimensionless friction force can be altered. Therefore, the non-dimensional fluid pressure change, $\hat{P}_i$, can play the role of *input*, u, into the dynamical system (see Equation (1)). By controlling this input, according to the theory presented in Section 2, we can stabilize the system, as shown in Sections 3.3–3.4. Deviations from Terzaghi principle can be considered as uncertainties and unmodeled dynamics that robust control should tackle (see also Section 2.3.4).

3.2. Self-Organized Critical Behavior

The term *Self-Organized Criticality* (SOC) was coined in 1988, in the seminal paper of Bak et al. (1988) (see also Bak & Chen, 1989), in order to describe the emergence of a critical state in dissipative, dynamical systems, which have no intrinsic time or length scale. The analysis of Bak et al. (1988) is based on a cellular automaton (Wolfram, 1983), in which a particle is added to a randomly selected cell in a square grid of cells. When a cell in the grid accumulates four particles, the particles are redistributed to their neighboring cells or they are lost (deleted), if they exceed the grid. This conceptually simple model leads to a behavior characterized by long periods of stasis (quiescence) interrupted by intermittent bursts of activity involving the avalanche of few or many particles. These instabilities follow a frequency-area power (fractal) distribution:

$$N \propto N_f^{-a}, \tag{28}$$

where N is the number of avalanches, N_f the number of particles involved in an avalanche, and $a \approx 1$.

A large class of systems is believed to exhibit *self-organized criticallity*. These systems are continuously in or close to a state of *marginal stability*, show *chaotic behavior* and obey to similar spatio-temporal correlations and statistical laws. GBK is such a system.

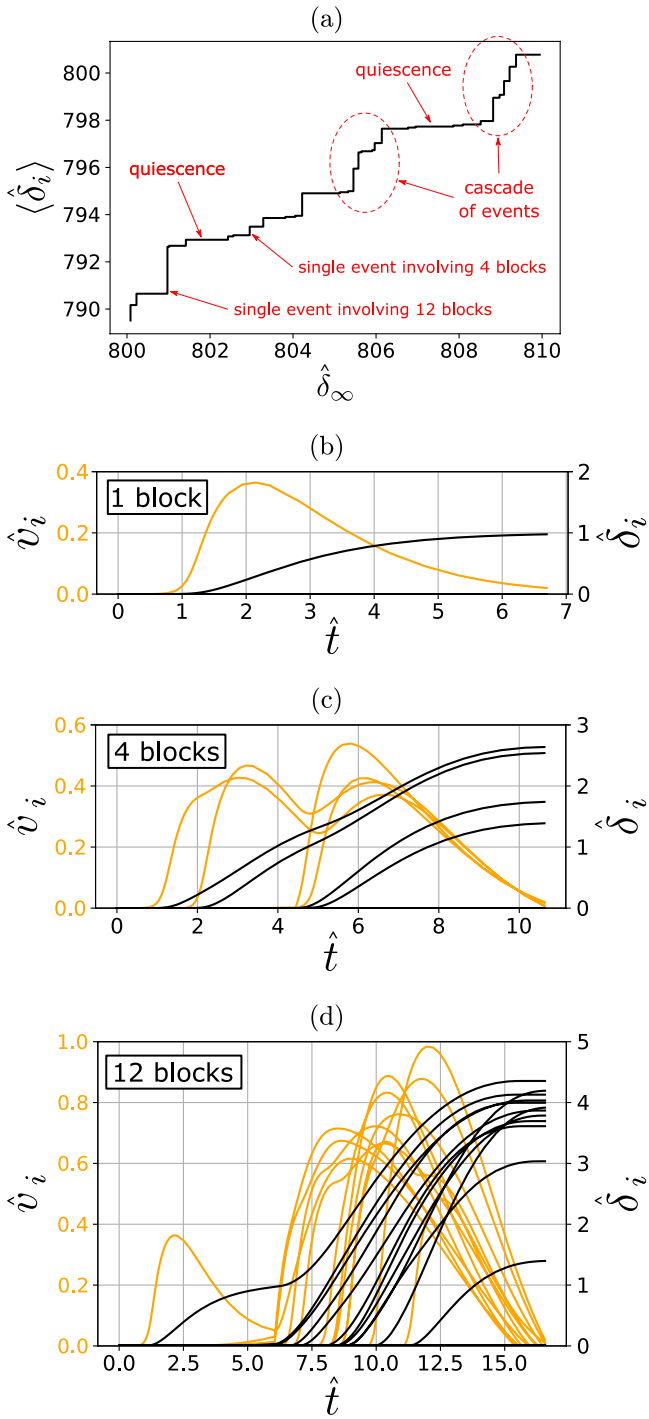

Figure 3. (a) Evolution of average dimensionless accumulated slip, $\langle \hat{\delta}_i \rangle = \frac{1}{n_b} \sum_{i=1}^{n_b} \hat{\delta}_i$ ($n_b = 24$), as a function of the dimensionless driver plate displacement, $\hat{\delta}_\infty$. The jumps correspond to fast, dynamic events of slip involving one or several blocks (avalanches). Cascade or single events are preceded by large periods of quiescence (plateaus), where energy is accumulated into the system due to the slow movement of the driver plate (b-d) Examples of the sudden, unstable sliding of a single block, of four blocks, and of 12 blocks (out of 24), respectively. Dimensionless slip, $\hat{\delta}_i$, and slip-rate, $\hat{v}_i$, are reported.

In order to illustrate the SOC behavior of GBK models and later control it, we simulate the behavior of a chain of twenty-four ($n_b = 24$) blocks. We let our simulations run until $N_0 = 10,000$ events of abrupt sliding are recorded, corresponding to $\hat{\delta}_\infty \approx 3300$ (details of the simulation procedure are given in Appendix B). $\hat{\delta}_\infty$ denotes the dimensionless displacement of the driver plate (see Figure 2). In Figure 3a, we present the evolution of the dimensionless accumulated slip $\hat{\delta}_i$ of the blocks (averaged over their total number) with respect to $\hat{\delta}_\infty$. Each step in this plot corresponds to a dynamic event of abrupt sliding of either a single, a cluster or of all the blocks of the system. The magnitude of the observed jumps in displacement depends on the number of the involved blocks in each event. Before an event, a period of quiescence is observed. During this period, the energy is progressively stored in the springs and no slip takes place (see plateaus in Figure 3a). Then, the system becomes again unstable and sudden slip occurs. In this sense, the system is always driven toward a state of marginal stability.

Figures 3b–3d depict slip events involving a single block and clusters of blocks of various sizes. Often, large events start with the sliding of only one or a couple of blocks, which push their neighbors to sliding in a similar way to a chain reaction (see Figures 3c and 3d). The reported slip velocities are high, compared to the slow time scale of the movement of the driver plate and its overall dynamical behavior is rich and complex.

As shown in Figure 4, the frequency $\left(\frac{N}{N_0}\right)$ as a function of the number of blocks involved in a slip event (N_f) is found to satisfy the power law distribution with $a \approx 1.5$. Similar exponent values were found for different frictional laws and for larger systems of blocks with higher interconnectivity (see Brown et al., 1991; Carlson & Langer, 1989; Huang et al., 1992; Narkounskaia et al., 1992; Rundle & Brown, 1991; Turcotte, 1999, among others). For these large events, the necessary conditions for SOC behavior, which are detailed in the Discussion (Section 5.1), do not hold and the system is not representative of SOC anymore. Nevertheless, our control strategy is designed/applied in such a way (see Sections 3.3, 3.4 and 4) as to be always effective independently of the size of the events, the statistics of the uncontrolled system and its complexity.

3.3. Stabilization

We use the theoretical developments presented in Section 2.1 for stabilizing the system and extend the periods of stasis as long as desired. In this way abrupt energy releases due to sudden sliding will be prevented.

For the design of the controller and for the numerical examples presented below, we need to consider a reference friction and a reference frictional weakening which are lower than the possible minimum friction and higher than the frictional weakening of the blocks (see Equations (4)–(5)), respectively. Based on the theoretical developments of Section 2 and despite uncertainties related to friction, the controller will manage to unravel in real time the unknown dynamics of the system and stabilize it by increasing or decreasing the fluid pressure in the required rate for assuring stability.

Figure 5 shows an example of stabilization of the system. In this example, the controller was activated after the initiation of unstable sliding of the two over the four blocks presented in Figure 3c (see red star symbol). This was done for illustrating the capabilities of our approach. We observe that the control-

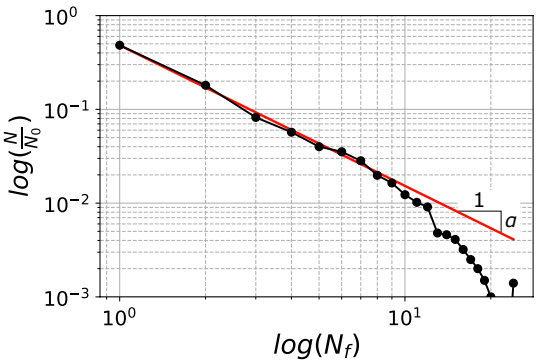

Figure 4. Power-law distribution of the frequency $\left(\frac{N}{N_0}\right)$ as a function of the number of blocks involved in slip events (N_f) per avalanche. The power law exponent is equal to $a \approx 1.5$.

ler automatically reduces the fluid pressure at the interfaces of the sliding blocks (Figure 5b) and succeeds in immobilizing them as shown in Figure 5a. If the controller is activated before the sliding event, then the instability is completely avoided by tiny decreases in the pressures of the frictional interfaces of the blocks having the tendency to slide (unstable blocks) and their neighbors. The pressure changes in this case are that small that is not worth of plotting. It should be emphasized that this stabilization is achieved without the controller knowing the exact rheology and the frictional properties of the system.

As far as the controller can maintain the pressure, the system will be stable and no instability (sudden sliding and energy relaxation) will take place. However, if the controller is deactivated, the system will slide abruptly and its unstable character will be restored. Therefore, there is a need to drive the system toward a new, stable equilibrium in a stable, smooth, quasi-static way.

3.4. Driving the System to Lower Energy Levels Without Abrupt Slip Events

Once a stabilizing, robust controller has been designed, it can be extended in order to make the blocks move to a desired new position with a desired velocity. The mathematical extension of the stabilizing controller to tracking was presented in Section 2.2 and it is robust, meaning that it can drive the system in a controlled manner and in the absence of complete knowledge of its parameters and physics.

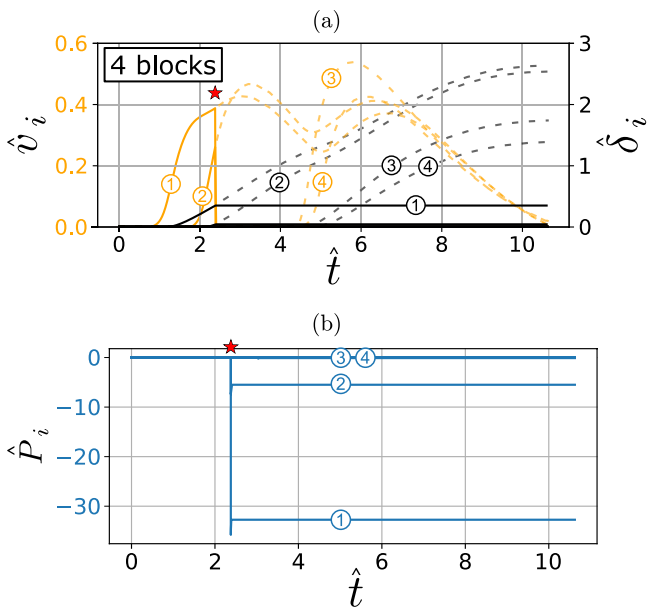

Figure 5. (a) Stabilization of the unstable movement of blocks as presented in Figure 3c. The controller was activated at $\hat{t} = 2.4$ (red star symbol) and successfully stabilized the system by arresting slip. Solid lines show the evolution of non-dimensional slip and slip-rate of the sliding blocks. Dashed lines show their movement without the controller. (b) The input pressure at the frictional interfaces of the blocks is automatically regulated by the controller. Zero $\hat{P}_i$ corresponds to no fluid pressure change, positive to pumping of more fluid and negative to fluid withdrawal. All quantities are dimensionless (see Appendix A).

In order to illustrate how the controller guides the system to a new position, we focus on the avalanche involving 12 unstable blocks, as presented in Figure 3d. During this event, the total potential energy change, which is calculated as the sum of the potential energy change of the springs, was $\Delta\mathcal{E}_U \approx -100$ (dimensionless). This drop in potential energy happens extremely fast. The maximum velocities reported during the movement of the unstable blocks was of the order of $\hat{v} \approx 1$ (see Figure 3d). Two *control strategies* will be investigated for guarantying at least the same drop in potential energy, but smoothly, without any unstable, uncontrolled movement of any block.

In the first control strategy, the controller will adjust automatically the input pressure in order to assure translation of all the blocks under the same constant velocity, which is chosen to be equal to $\hat{v}_d = 2 \times 10^{-3}$ (dimensionless). This target velocity is three orders of magnitude lower than the maximum velocity developed during the unstable movement (see Figure 3d), but several orders of magnitude higher than the normalized far-field driving velocity, $\hat{v}_\infty$. We allow the system to evolve for a total time equal to $\hat{t}_d = 2000$. In Figure 6, we present the evolution with time of the dimensionless displacements and velocities of all the blocks, the non-dimensional input pressure determined by the controller, the dimensionless potential energy drop and the energy dissipation due to friction. We observe that the controller succeeds in regulating the velocity of all the blocks to the desired value. A small overshoot in velocities at the beginning of the controlled sliding is related to the parameters of the controller chosen (see Equation (7)). This overshoot can be optimized depending on the desired rate of input pressure change.

At the beginning, the applied pressure change is zero, but the controller adjusts it automatically, in order to allow for the blocks to attain the desired velocity, as shown in Figure 6b. Two groups of blocks are distinguished, that is, those that are on the verge of unstable movement and those that are in a stable equilibrium. In the case of the former, we observe that the input pres-

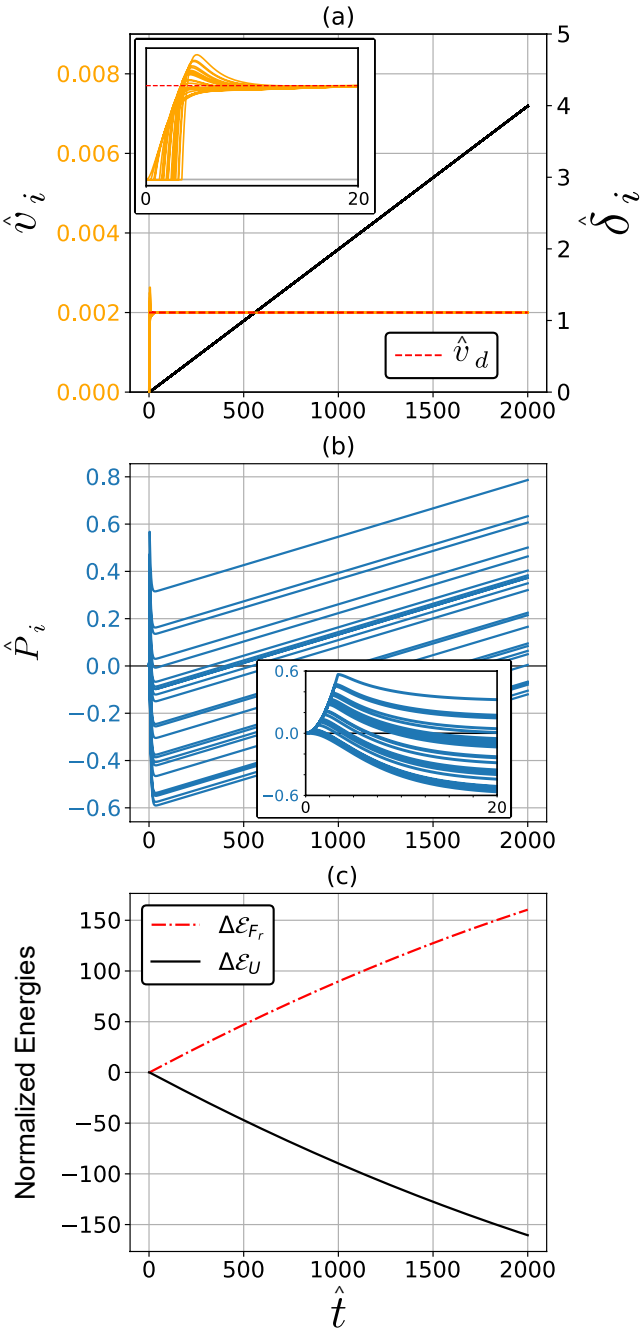

Figure 6. First control strategy: time evolution of (a) the displacements, $\hat{\delta}_i$, and velocities, $\hat{v}_i$, of all the blocks, (b) the input pressures, $\hat{P}_i$, determined by the controller and (c) the total potential energy drop, $\Delta\mathcal{E}_U$, and the energy dissipation due to friction, $\Delta\mathcal{E}_{F_r}$. We observe that the controller succeeds in regulating the velocity of all the blocks to the desired value, $\hat{v}_d$, and dissipate the total potential energy in a controlled and smooth manner, avoiding any instabilities. All quantities are dimensionless (see Appendix A).

sure is decreased (negative pressure change; fluid withdrawal). As a result the regulator increases friction, decelerates the movement of the blocks and stabilizes the system. On the contrary, in the case of the latter, the controller increases the input pressure in order to accelerate their motion and achieve the desired target velocity.

It is worth emphasizing that the regulator is not based on any "if-then" statements - this would be impossible in general situations. On the contrary, based on the mathematical developments presented in Section 2.2, it automatically regulates the fluid pressure of the blocks and stabilizes the system by unraveling its dynamics in real time. This is accomplished by monitoring the motion of the system and adjusting the input pressures changes in real-time (see Figure 1).

Regarding the blocks that started from a stable equilibrium, at a certain point they also enter to a critical state due to slip and strain accumulation in the springs. At that point, we observe that the controller decreases their input pressure, in order to alter the dynamics of the system, guarantee stability and achieve motion under the desired velocity. This is depicted in Figure 6b by the negative pressure change at all the blocks (pressure reduction).

The stored energy in the system is dissipated almost linearly with time as shown in Figure 6c. The same holds for the potential energy decrease in the system. Notice that thanks to the desired very low target velocities, the kinetic energy of the system and the viscous dissipation are negligible compared to the drop in potential energy. With our approach, we finally manage to dissipate more than the released energy during the unstable, abrupt movement of the system, but in a slow, smooth and controlled manner. Consequently, the system is not anymore in a state of a marginal stability and it cannot present a self-organized critical behavior (Ben-Zion, 2008). Moreover, as its motion is actively controlled, no chaotic behavior can be observed. In other words, we managed to completely alter the dynamics of the system in a desired way.

However, the results show that the controller has to assure a negative input pressure in order to prevent the unstable movement of some blocks (see Figure 6b). These (lower than the initial) pressures have to be maintained for assuring stability. Therefore, if we decided to deactivate the controller, the system would become again unstable. Nonetheless, it is possible to bring it in a state of stable equilibrium, in which the controller will be no more necessary and will be possible to deactivate it safely. For this purpose, we follow a different scenario and instead of setting the velocity of each one of the blocks to the desired velocity, we set the average velocity equal to $\hat{v}_d = \langle \hat{v}_i \rangle = \frac{1}{n_b} \sum_{i=1}^{n_b} \hat{v}_i = 2 \times 10^{-3}$. In this manner, we incite a faster, but controlled movement for the unstable blocks for which the input pressure is negative. As a result some blocks move faster than others, noting higher displacements (Figure 7a). After some time, we observe that the blocks self-tune and slide with identical slip-rates equal to the desired one. Once more, the system's dynamics were altered and no self-organized critical or chaotic behavior occurred. On the contrary, we incited the system to self-organize toward a stable equilibrium (see $\hat{t} > 1200$ in Figure 7). This is indicated by the positive input pressures changes at the frictional interfaces of all the blocks, which are required to sustain the movement under the desired average velocity.

In order to illustrate the stability of the system in this new state, we decide to progressively deactivate the controller between $\hat{t} = 1250$ and 1750, as depicted in Figure 7. After deactivation, the system remains in a state of stable

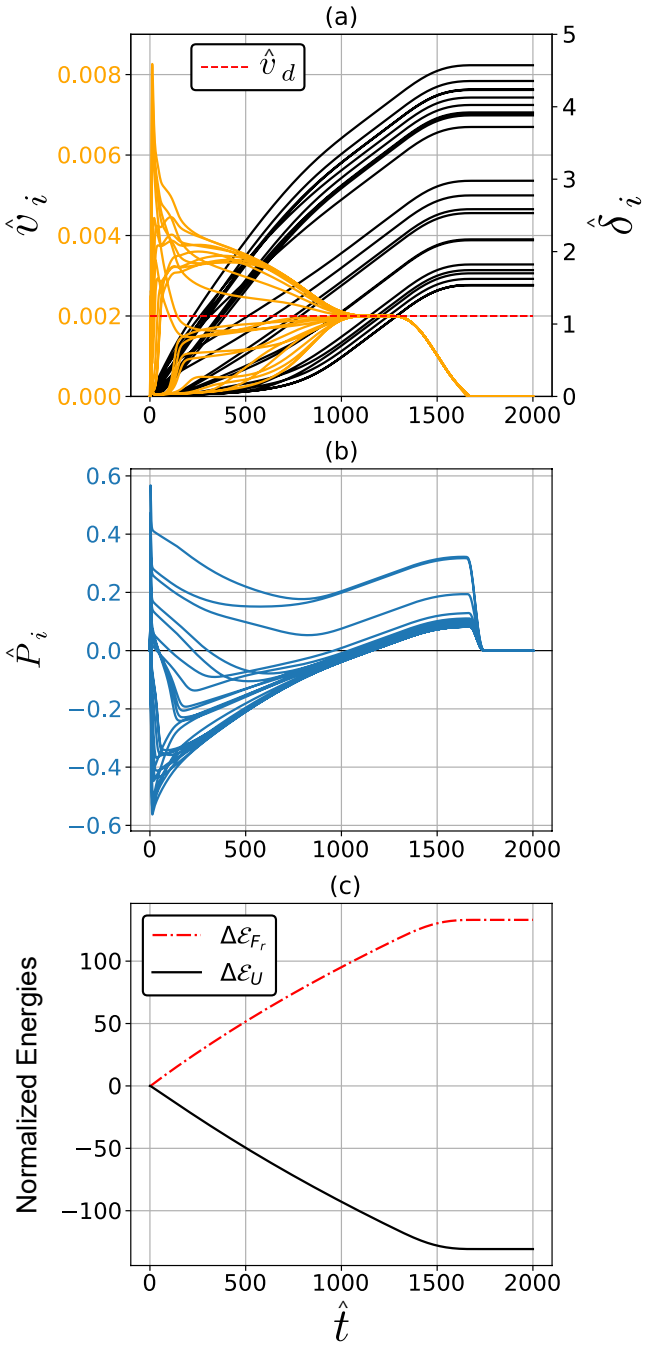

Figure 7. Second control strategy: time evolution of (a) the displacements, $\hat{\delta}_i$, and velocities, $\hat{v}_i$, of all the blocks, (b) the input pressures, $\hat{P}_i$, determined by the controller and (c) the total potential energy drop, $\Delta\mathcal{E}_U$, and the energy dissipation due to friction, $\Delta\mathcal{E}_{F_r}$. We observe that the controller succeeds in regulating the average velocity of the blocks to the desired value, $\hat{v}_d$. The blocks self-organize to a desired stable equilibrium state. Then, after $\hat{t} = 1250$, the controller is progressively deactivated. Any instabilities are prevented and the total potential energy is dissipated efficiently, as desired. All quantities are dimensionless (see Appendix A).

equilibrium of a lower (potential) energy level. Of course, if the controller remains inactive, the continuous slow movement of the driver plate will render again the system unstable after a (large) time interval. Therefore, it might be interesting after this point to set the controller's target velocity equal to the driver plate's (far-field) velocity. In this case the regulator will automatically adjust the fluid pressure and the blocks will follow the movement of the driver plate sliding continuously in an aseismic way applying only small pressure changes.

The above numerical examples show that the system is finally stabilized by reducing the pressure at the blocks' interfaces and not by increasing it. This might be at first counter-intuitive, if stabilization is thought as a simple process of adjusting pressure in order to satisfy the frictional stability condition of the system. Notice that for the single spring-slider model, frictional stability is guaranteed when the stiffness of the loading system is higher than a critical softening stiffness, which depends on the exact frictional parameters and rheology (see Ruina, 1983; Scholz, 2019; Stefanou, 2019). For the GBK model, the stability conditions are qualitatively similar. Nevertheless, attempting to stabilize the system by satisfying the frictional stability conditions (provided that the fault is reactivated) would require very high positive fluid pressure changes. Moreover and most importantly, the path from low to high pressure may trigger instabilities and cascade failure. On the contrary, with our approach, we achieve stabilization with minimal pressure changes. Additionally, we guarantee controlled sliding, with a desired target velocity profile.

4. Controlling Seismic Slip of Faults

In this Section, we present an example of the theoretical developments presented in Section 2 for the control of the seismic activity of a strike-slip fault (see Figure 8a). In this academic example, the fault is just beneath the surface (see Figures 8b and 8c) and its dimensions are 5×5 km^2 (x- and z-directions, respectively). The effective normal stress acting on the fault interface is assumed to vary only with depth as shown in Figure 8b. We assume also that the fault is adequately oriented in the tectonic stress regime for slip to occur.

As far as it concerns the frictional properties of the fault area, the truncated version of the RSF law was considered using the aging law for the evolution of the state (see Section 2.3.3 and Equation (21)). The parameters a, b and d_c are spatially distributed using a log-normal distribution with average $a^{\text{avg}} = 0.010$, $b^{\text{avg}} = 0.015$ and $d_c^{\text{avg}} = 10$ mm and standard deviation corresponding to 5% of the average values (see Figure 8c). The parameters are kept constant over each element of the discretization during the simulations. This stochastic distribution of the frictional parameters over the fault area represents heterogeneities that exist in real faults and show that the proposed control approach is insensitive to this kind of uncertainties.

The fault area is discretized into $N_x \times N_z = 30 \times 30$ elements. This discretization is fine enough as the elements have a characteristic size of 0.167 km, which is sufficiently lower than the minimum nucleation size, $h^*_{\text{min}} = 0.407$ km. The nucleation size over the fault area is illustrated in Figure 8d. It is calculated as $h^* = \frac{2}{\pi} \frac{G d_c}{(b-a)\sigma'_{zz}}$ (see Rice, 1993). $G = 30$ GPa is the elastic shear modulus of the surrounding rocks. If one considers the average for the RSF

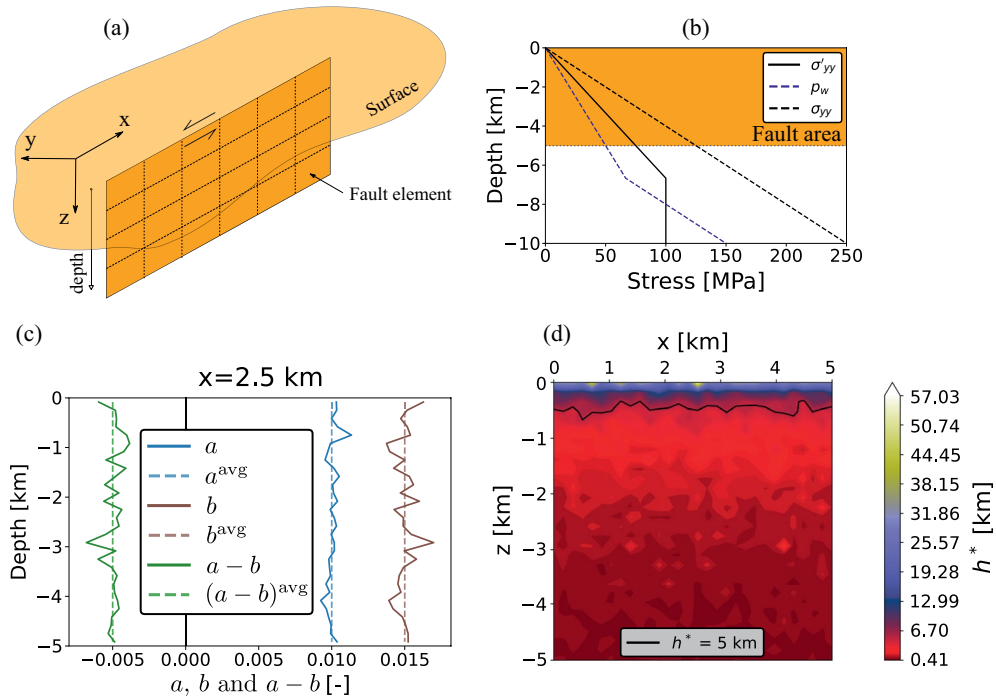

Figure 8. (a) Sketch of a strike-slip fault configuration discretized in $N_x \times N_z$ elements. (b) In-situ pore fluid pressure p_w (hydrostatic), in-situ normal stress σ_{yy} and effective normal stress σ'_{yy} as a function of depth (x-direction invariant). (c) Spatially distributed rate-and-state frictional parameters a, b and $a-b$ (solid lines) along with their respective averaged values (dashed lines) as a function of depth at fixed x = 2.5 km. (d) Contour plot illustrating the distribution of nucleation size (activation length) over the fault area due to statistical heterogeneities. The black contour line depicts the region in the fault where the nucleation size is equal to $h^* = 5$ km.

parameters, then the average nucleation size over the fault surface is equal to $h^*_{\text{avg}} = 1.02$ km, which is smaller than the equivalent length of the fault (5 km). As a result, the system is unstable and a dynamic event is expected. In addition, a constant slip-rate at depth was assumed of the order of 1 cm/yr to load the system.

In Figures 9a and 9b, we present the average response of the strike-slip fault for a single (isolated) typical dynamic event. The maximum reported velocity (averaged over the fault surface) is 0.35 m/s corresponding to a maximum slip of 1.2 m (Figure 9a). This dynamic event is associated with a stress drop of approximately 10 MPa (Figure 9b) resulting to an earthquake of magnitude $M_w \approx 6$.

The difference of this example with the Burridge-Knopoff model, presented in the previous Sections, is the long-range interactions along the points of the fault area. The elastodynamic equations of motion are discretized using the approach described in Rice (1993); Chinnery (1963) (see also Figure 8a). This leads to a full matrix A. Notice that one could also design the controller using a simplified band matrix emerging from the 1D or the 2D GBK approximations. In this case, the non-zero, off-diagonal terms would have to be considered as uncertainties, according to the theoretical developments presented in Section 2. However, in this example, we consider the full matrix A corresponding to the exact strike-slip configuration, even though a diagonal one could be sufficient too for its control (see Equation (5)). For the simulations presented in this Section, a dynamic approach has been employed, adopting a lumped mass matrix in order to represent the mobilized mass during a seismic event. Other formulations are of course possible (see Erickson et al., 2020, among others).

It is worth emphasizing that several methods can be used in order to discretize the differential operator representing the underlying continuum elastodynamic problem of seismic slip (e.g., Finite Element Method, Finite Differences, Boundary Element Method, spectral methods, model reduction methods, among others (see Barbot, 2019; Boyd, 2000; Erickson et al., 2020; Larochelle et al., 2021)). In most cases, the resulting discretized equations will finally take the form of Equations (1) and, consequently, the control theory presented in this work can be applied.

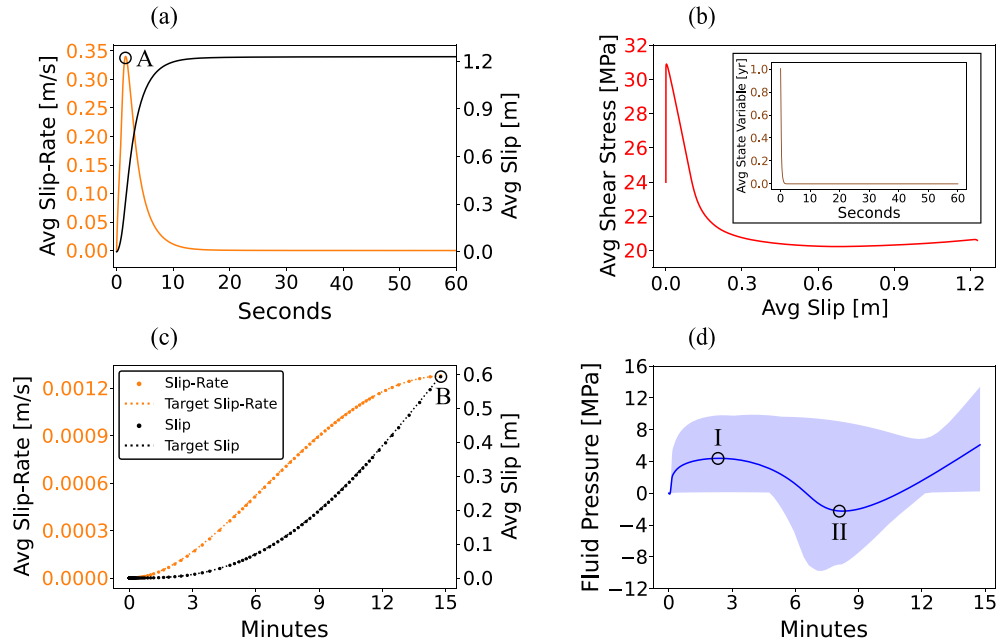

Figure 9. 1st row: Open-loop response of the strike-slip fault for a single dynamic event. (a) Average slip (black) and slip-rate (orange) in terms of time. (b) Corresponding average shear stress evolution in terms of slip. Inset: Average Rate-and-State Friction state variable in function of time. 2nd row: Closed-loop response of the strike-slip fault after the application of the controller. (c) Average slip (black dotted curve) and slip-rate (orange dotted curve) in terms of time. The controller successfully achieves the target/reference slip (black dashed line) and slip-rate (orange dashed line). (d) Evolution of the average applied fluid pressure change (output of the controller). The blue shaded area corresponds to the envelope of pressures developed over the surface of the fault.

In order to release the stored elastic energy and drive the fault to a new equilibrium point of lower energy, we apply the theory described in Section 2. As shown in Section 2.3.3, RSF is a Lipschitz function and, therefore, it can be bounded by the states of the system (i.e., the slip and the slip-rate). According to the bounds found in Section 2.3.3, the controller is designed with uniform frictional properties, even though the frictional system to control is heterogeneous. In other words, we do not need to know the exact frictional parameters and rheology of the fault in order to stabilize its slip and release aseismically the accumulated energy.

For tracking, we set a low velocity as reference/target trajectory, which, on average over the fault area, evolves smoothly from the far-field tectonic velocity (cm/yr) to approximately 1.5 mm/s (see Figure 9c). In this way, a new equilibrium point of lower energy is given as a target. Alternatively, the strategy presented in Section 3.4 could be used for setting the average target slip velocity. The duration of the control operation is set equal to $t_{op} = 15$ min.

In Figures 9c and 9d, we show the average response of the fault after the application of our controller. The evolution of slip and slip-rate, in Figure 9c, follows, as expected, the design/target slip-rate. From this plot, we can conclude that the fault can be driven into its designed new equilibrium point aseismically. In the example presented here, the maximum average slip velocity developed was approximately two orders of magnitude smaller than the earthquake event (0.35 m/s) presented in Figure 9a. Notice that the system was controlled in a relatively fast operation time (15 min). In case an even slower transition is needed, the reference trajectory and/or the operation time can be adjusted as desired.

In Figure 9d, we present the evolution of the average over the fault area fluid pressure change as a function of the operational time (output of the controller versus time). The controller regulates automatically the fluid pressure in order to achieve the reference/target slow slip. We chose to activate the controller on the verge of the unstable seismic event, in order to model the worst case scenario. If the controller was activated before, then the regulated fluid pressure change would follow a smoother evolution.

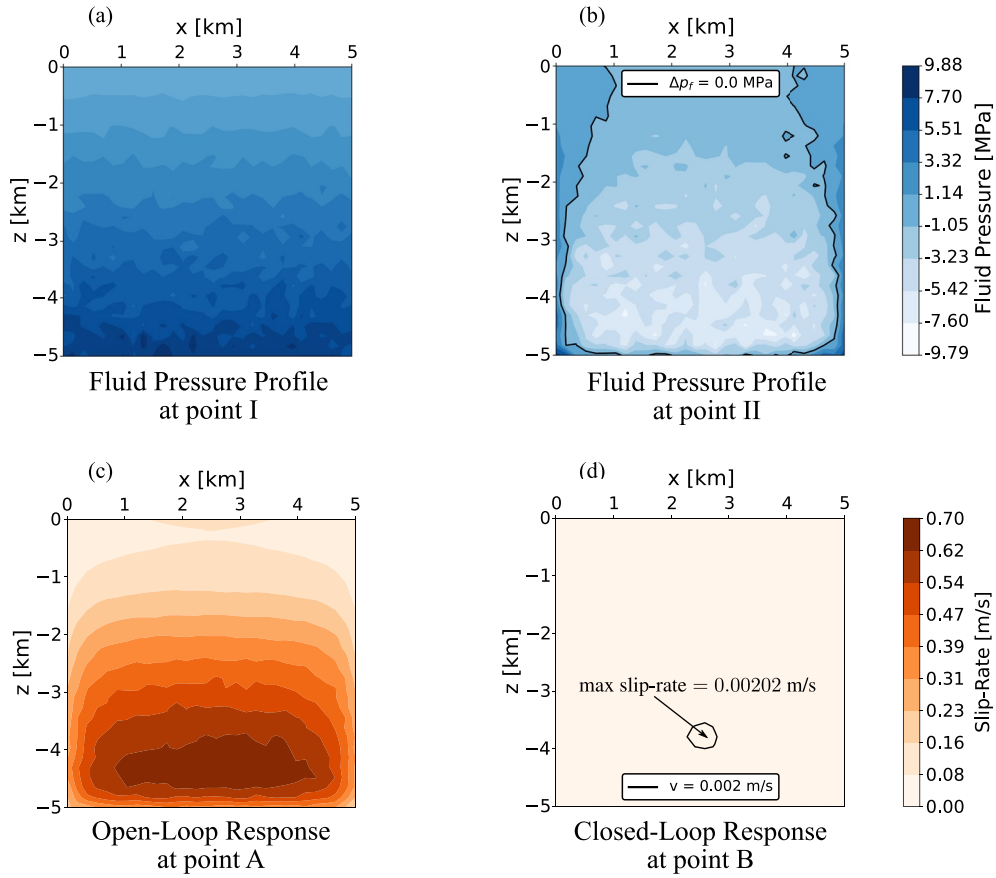

Figure 10. 1st row: Fluid-pressure change profile (output of the controller) over the fault at two distinct time instances, (a) at the maximum average fluid pressure change (point I in Figure 9d) and (b) at the minimum average fluid pressure change (point II in Figure 9d). See also supplementary material Movie S2 for an animation. 2nd row: Comparison of slip-rate distribution along the strike-slip fault between the open-loop, uncontrolled (c, see also supplementary material Movie S1 for an animation) and the closed-loop, controlled (d) system. The open-loop snapshot (c) is taken at the maximum developed average velocity during the earthquake event (point A in Figure 9a), while the closed-loop one (d) at the maximum developed average velocity during the applied control strategy (point B in Figure 9c).

We observe that at the beginning of the operation, that is, from $t = 0$ to $t \approx 2.5$ min, the controller increases the fluid pressure (positive fluid pressure change) in order to accelerate sliding from the far-field velocity to the target slip-rate. The fluid pressure profile over the fault at the maximum average pressure (point I in Figure 9d) is illustrated in Figure 10a. We can observe that pore pressure changes are positive (fluid injection) everywhere on the fault. Then, from $t \approx 2.5 - 8$ min, the regulator automatically decreases the pressure (negative fluid pressure change), in order to stabilize the system and avoid run-off. The fluid pressure profile over the fault at the minimum average pressure (point II in Figure 9d) is illustrated in Figure 10b. We can observe that the maximum negative fluid pressure changes (fluid withdrawal) occur at the bottom-middle of the fault area. Next, from $t \approx 8 - 12$ min, the controller gradually restores the pressure. Finally, positive fluid pressure changes are observed from $t \approx 12$ to $t = 15$ min for guarantying the continuation of creep-like, aseismic slip with the target slip-rate. In this last part of the operation, all the elements of the fault have entered in a (dynamically) stable state of lower energy and the controller could be deactivated. This behavior is qualitatively similar with the one obtained in Section 3.4 for the GBK model.

In this example, the fluid pressure changes vary between −10 (fluid withdrawal) and +10 MPa (fluid injection), approximately (see Figures 9d and 10a–10b). Notice that if one wanted to stabilize the system by simply satisfying the stability condition emerging from the expression of the nucleation length (assuming that the frictional parameters are somehow known), then the average fluid pressure should be immediately increased to approximately 68 MPa in order to achieve a resulting effective normal stress equal to approximately 6 MPa. But even if

this was possible, the slip-rate would be still unmanageable (in the best case scenario, it would be equal to the far-field tectonic velocity) and, most importantly, the rapid increase of the fluid pressure could trigger a rupture event (see also Tzortzopoulos et al., 2021).

A comparison between the open-loop, uncontrolled system and the closed-loop, controlled one is given in Figures 10c and 10d, in terms of slip-rates. Both figures display the spatial distribution of the slip-rates at times corresponding to the maximum average slip-rate of each simulation (i.e., at points A and B, see Figures 9a and 9c, respectively). The maximum developed slip-rate of the controlled system is 0.002 m/s (see black contour line, Figure 10d), which is negligible compared with the slip-rate developed during the simulated earthquake instability (0.7 m/s, approximately, see Figure 10c).

This academic example shows how seismic instabilities can be prevented and how controlled, slow-slip can be induced by fluid pressure adjustment, using the theory developed in this work. However, in this example the fluid pressure has to be adjusted independently over the elements of the fault area and diffusion phenomena are not considered. On one hand, these phenomena can introduce a delay to the closed-loop system, but, on the other hand, can allow to cover large fault areas with limited number of wells for optimal control. This limitation of the current approach together with other limitations are discussed in Section 5.4, where also perspectives are given.

5. Discussion and Concluding Remarks

5.1. Self-Organized Criticality Control

SOC could be seen as a spectacular manifestation of order in nature that results in sparks of energy relaxation (dissipation). Nonetheless, this does not mean that SOC behavior cannot be prevented. The necessary and sufficient conditions for SOC that were recently proposed by Watkins et al. (2016) and are presented below, leave open this possibility.

Self-Organized Criticality Control (SOCC) can be of particular importance in many situations where avalanches due to SOC behavior are unwelcome. SOCC is a relatively new field. Maybe the most popular example of SOCC is the prevention of large snow avalanches, by triggering smaller ones (Birkeland & Landry, 2002; McClung & Schaerer, 1993). Cajueiro and Andrade (2010a); Cajueiro and Andrade (2010b, 2010c) applied and extended this idea for controlling self-organized criticallity in the Abelian sand pile model (Dhar & Ramaswamy, 1989) and generalizations of it. Brummitt et al. (2012) studied the suppression of cascade failures in interconnected power-grids, based on the sand pile model of Bak et al. (1988). Again using as model the classical sandpile automaton of Bak et al. (1988), Noël et al. (2013) proposed a control strategy that determines the grid cell in which a particle should land in order to adjust the probability of triggered cascades and mitigate large avalanches. Another example of SOCC is given by Hoffmann and Payton (2014), who altered the SOC power law statistics of electrical circuits obeying Kirchoff's law, by adequately modifying the interconnectivity of the circuit network. In this way they proposed mitigation strategies of large cascade events.

According to Watkins et al. (2016), a system has to satisfy the following three *necessary* conditions in order to qualify as SOC:
NC1. Non-trivial scaling.
NC2. Spatio-temporal power law correlations.
NC3. Apparent self tuning to the critical point.

These necessary conditions are considered in the logical sense. In other words, a system cannot exhibit SOC if any of the above three conditions is not fulfilled.

An extensive discussion of the meaning of critical point and criticality in the frame of SOC and its connection with existing notions in physics and statistical mechanics is made in Watkins et al. (2016). Here, critical points are points in the phase portrait of the system that are (Lyapunov) unstable. Focusing on the GBK approximation, due to the slow driver plate's movement, the system is evolving continuously toward a critical, unstable equilibrium. This equilibrium is then followed by abrupt cascade events (non-equilibium states in the mathematical sense, see also Figure 3a). These events may be small, involving few blocks or large, involving several blocks.

Watkins et al. (2016) give also the following three *sufficient* conditions for characterizing a system as SOC:

SC1. Non-linear interaction, normally in the form of thresholds.
SC2. Avalanching.
SC3. Separation of time scales.

That means that if a system fulfills these conditions, then it exhibits SOC.

The open-loop, uncontrolled GBK model, $\Sigma(P_\ell)$, satisfies all the sufficient conditions and therefore exhibits SOC. In particular, friction introduces the necessary non-linearities and it takes a maximum value before slip initiation (threshold). Avalanches are also observed involving clusters of blocks that dissipate abruptly the energy of the system (intermittent energy relaxation). The driver plate's slow movement introduces a slow time scale in $\Sigma(P_\ell)$ (cf. Time-scale asymptotic analysis in Stefanou (2019)), while the events follow the fast characteristic times related to the frictional instability during avalanches.

In contrast, the controlled, closed-loop system, $\Sigma(P_\ell, C)$, remains strongly non-linear, satisfying condition SC1, but not conditions SC2 and SC3. Moreover, it does not satisfy the necessary condition NC3, because our controller, $\Sigma(C)$, is designed to prohibit self-tuning to a critical point. Instead, the closed-loop system is self-tuned toward desirable stable equilibria. As a result, based on the necessary conditions of Watkins et al. (2016), the controlled system cannot exhibit SOC. Self-organized criticality is controlled.

It is worth pointing out that our control approach differs from the aforementioned SOCC approaches in many aspects. First of all, it is based on a totally different mathematical framework. This framework allows us to derive rigorous mathematical proofs about the stabilization and controllability of the non-linear system. Moreover, it allows to alter its dynamics by considering also the uncertainties of the physical model (robustness) in a deterministic way. Additionally, we don't trigger any instabilities to dissipate energy, as it is done in the above cited works, and we do not artificially increase locally the energy of the system or change its interconnectivity by using statistical methods. In this sense, our approach is deterministic even though it considers the uncertainties of the underlying physics. As a result, we go beyond existing SOCC approaches by slowing down the dynamics of the GBK model. In this way, we do not only dissipate the required energy in a controlled manner, but we also break the separation between slow and fast dynamics of the system, which is key ingredient for SOC as stated above.

5.2. Restriction of Chaotic Behavior

Chaotic behavior is also restricted. While the evolution of the uncontrolled underlying dynamics in the above applications might be chaotic and could be predictable only in a statistical sense, the evolution of the controlled system is not. The presence of the controller guarantees global asymptotic (exponential) stability (see Section 2.1). Hence no limit cycles or chaos are possible. Moreover, the controller is robust, meaning that it succeeds in altering the dynamics of the system even without knowing its exact properties. Indeed, only some rough boundaries of the governing parameters are needed in order to drive and control the system as desired.

5.3. Implications for Complex Geo-Systems

Having the possibility of controlling the dynamics of a complex system in a robust way can give us useful information about its inherent, but practically inaccessible properties. Here, we drive smoothly the studied dynamical systems to new states. By back-analyzing the evolution of the stabilizing input (i.e., pressure change), one could draw real-time conclusions about the elasticity, the friction, the dynamics and other (unobservable) characteristics of the underlying system. Therefore, the proposed strategy could help in improving the current understanding and help in data mining and system identification in some frictionally unstable geo-systems that complexity makes opaque.

An additional implication of the proposed theory has to do with *predictability*. Predicting the evolution of complex systems exhibiting self-organized critical behavior (or richer) is a challenging, but controversial topic (see Ben-Zion, 2008; Sornette, 1999; Watkins et al., 2016, for an overview). Nevertheless, the ability to predict can have important consequences in many disciplines (cf. Earthquakes, tectonics, volcanoes). The distribution and frequencies of cascade failures is a useful statistical correlation. However, it cannot provide with certainty when and how large exactly the next cascade failure will be. Nevertheless, if control is possible then prediction is less central. The more we control a system, the less unpredictable it becomes. Of course, one would need

sufficient inputs and monitoring for guaranteeing full control (see *controllability* and *observability* notions of the mathematical Theory of Control in Khalil, 2015, among others). However, even if only partial control is possible (e.g., due to limited area of intervention and technological constraints), the space of uncontrolled dynamics will be reduced, which can lead to improved predictability (e.g., increase the predictability horizon (e.g., Gualandi et al., 2020)) and constrain the size of the next cascade event.

5.4. Implications for Anthropogenic and Natural Earthquakes and Current Limitations

A direct implication of the present work is inevitably related to earthquakes and induced/triggered seismicity. An interesting point of this mathematical framework is the possibility of deriving rigorous proofs about the controllability of the salient unstable dynamics of earthquake faults. Moreover, control is possible without knowing the exact properties of the system and its physics. For instance, the detailed knowledge of faults' frictional parameters, which is practically impossible to acquire in practice, is not a sine qua non condition. Notice that friction is a major unknown (Erickson et al., 2011) in earthquake science. However, our control approach needs minimal and not precise information about the frictional characteristics of the fault system, which can be acquired in practice. Based on this limited information, we show how the system can be driven to a new state of lower energy in a totally controlled and aseismic way. Moreover, our approach guarantees aseismic, slow-slip and smooth energy relaxation and does not require the knowledge of the exact current stress state and tectonic setting. Finally, the system is controlled independently of being far or close to its critical points, that is, to an earthquake event.

Without any doubt, claiming that controlling anthropogenic or natural seismicity is possible, based on the analysis presented herein, is a speculation and further research is needed. Several theoretical and techno-economical investigations have to be pursued further in order to show into what extent man-made or natural earthquakes can be prevented (or the opposite). For example, some direct limitations of the proposed theory have to do with the actual technological means for fluid injections in the earth's crust (e.g., number of wells, pressure limits of pumps, response time). In this case special analyses have to be performed to adjust the operation time and incorporate the limitations of the pumping system in the design of the controller.

The sampling-rate of the observations is also an important factor. Here, we presented examples of continuous time control, but, if the sampling-rate is low, discrete-time control is necessary. A first attempt toward the solution of this problem is presented in Papachristos and Stefanou (2021), where discrete-time dynamics are considered. Moreover, measurements of the state of the system are never free of errors. These errors can be considered as disturbances (Khalil, 2015) and tackled with other controllers that are more resilient and robust.

Diffusion phenomena and poroelastodynamic couplings were ignored in this work. These processes introduce time-delays, which can make the design of robust controllers more challenging and exceed the scope of the current work. For more details about the design of controllers under the effect of fluid diffusion, we refer to Tzortzopoulos (2021a); Tzortzopoulos (2021b). Moreover, in the current design, the controller had access to the full state of the system. In practice, this is impossible and robust observers (estimators) have to be designed.

Another open question is related to the fact that, even if it is proven feasible to control the rupture of a family of well-known faults, the rupture of unknown, adjacent faults is not excluded. For this purpose the design of non-local control approaches would be needed based on macroscopic/average measurements. Finally, extensive laboratory testing may be needed before applying the theory to real faults.

The above limitations and other open questions may inspire further research and give new perspectives on controlling induced and/or natural seismicity.

Appendix A: Equations of Motion of the GBK Model

The equation of motion of each block i with mass m_i, where $i = 1, 2, .., n_b$ with n_b to be the total number of blocks, is written as follows:

$$\begin{aligned} m_i \dot{v}_i = & \sum_{j=1}^{n_b} k_{ij}^c (\delta_j - \delta_i) + \sum_{j=1}^{n_b} \eta_{ij}^c (v_j - v_i) \\ & + k_i^l (\delta_\infty - \delta_i) + \eta_i^l (v_\infty - v_i) \\ & + \sum_{j=1}^{n_b} k_{ij}^c \left(\delta_j^0 - \delta_i^0\right) - F_i^r, \end{aligned} \tag{A1}$$

where $(\dot{.})$ is the time derivative, δ_i and v_i are, respectively, the slip (displacement) and slip-rate (velocity) of the block i, δ_∞ and v_∞ are, respectively, the displacement and velocity of the driver plate, which represents the far field tectonic velocity in the case of faults, and δ_i^0 is the initial displacement of the block i. k stands for stiffness and η for damping coefficients. The superscript 'c' denotes the springs and dampers between the blocks and the superscript 'l' the same elements between the blocks and the driver plate. For instance, k_{ij}^c is the stiffness coefficient of the spring connecting block i with block j, while η_i^l is the damping coefficient of the dashpot connecting the block i with the driver plate. F_i^r represents the friction of block i with the rough plane and can depend on slip, rate of slip and other internal state variables (see Section 2.3). Here, $F_i^r = F_i^r(\delta_i, v_i)$.

Setting $\omega^* = \sqrt{\frac{k^*}{m^*}}$, where k^* and m^* are, respectively, a reference stiffness and mass, the above equations take the dimensionless form:

$$\begin{aligned}\hat{m}_i \hat{v}_i' = &\sum_{j=1}^{n_b} \hat{k}_{ij}^c \left(\hat{\delta}_j - \hat{\delta}_i\right) + \sum_{j=1}^{n_b} 2\zeta \hat{\eta}_{ij}^c \left(\hat{v}_j - \hat{v}_i\right) \\ &+\hat{k}_i^l \left(\hat{\delta}_\infty - \hat{\delta}_i\right) + 2\zeta \hat{\eta}_i^l \left(\hat{v}_\infty - \hat{v}_i\right) \\ &+ \sum_{j=1}^{n_b} \hat{k}_{ij}^c \left(\hat{\delta}_j^0 - \hat{\delta}_i^0\right) - \hat{F}_i^r,\end{aligned} \tag{A2}$$

where $(.)'$ is the derivative with respect to the dimensionless time $\hat{t} = \omega^* t$, $\zeta = \frac{\eta^*}{2m^*\omega^*}$ is the damping ratio, $\hat{k}_x^{c,l} = k^{*-1} k_x^{c,l}$, $\hat{\eta}_x^{c,l} = \eta^{*-1}\eta_x^{c,l}$, $\eta^* = 2\zeta m^* \omega^*$, $\hat{\delta}_i = D^{*-1}\delta_i$, $\hat{v}_i = v_i D^{*-1}\omega^{*-1}$, D^* a reference displacement and $\hat{F}_i^r = (D^* k^*)^{-1} F_i^r$.

Equations (A2) are written in matrix form as follows:

$$x' = \underbrace{\begin{bmatrix} O_{n_b \times n_b} & I_{n_b} \\ -K & -2\zeta K \end{bmatrix}}_{A} x + \underbrace{\begin{bmatrix} O_{n_b} \\ \Psi \end{bmatrix}}_{h(x)}. \tag{A3}$$

The first n_b components of the state vector $x \in \mathbb{R}^{2n_b}$ represent the dimensionless displacements, $\hat{\delta}_i$, and the rest n_b components the dimensionless velocities of the blocks, $\hat{v}_i$. $O_{n_b \times n_b}$ and I_{n_b} are, respectively, the zero and identity matrices of size $n_b \times n_b$ and O_{n_b} the zero vector of size n_b. $K = M^{-1}\left(K^l - K^c\right)$, where M is a diagonal matrix containing the dimensionless masses of the blocks, $\{M\}_{ii} = \hat{m}_i = 1$, $\{K^c\}_{ij} = \hat{k}_{ij}^c$ and K^l a diagonal matrix with components $\left\{K^l\right\}_{ii} = \hat{k}_i^l$. In the above equation, we assumed that the dimensionless damping coefficients coincide with the dimensionless stiffnesses. This is a reasonable assumption in the absence of more detailed data. The vector Ψ represents the dimensionless forces applied to the blocks due to the initial deformation of the springs, $\hat{\delta}_i^0$, the displacement, $\hat{\delta}_\infty$, and velocity, $\hat{v}_\infty$, of the driver plate, and the friction forces $\hat{F}_i^r$:

$$\Psi = M^{-1}\left(-F^r - KU^0 + K^l U^\infty + 2\zeta K^l V^\infty\right), \tag{A4}$$

where $\{F^r\}_i = \hat{F}_i^r$, $\left\{U^0\right\}_i = \hat{\delta}_i^0$, $\{U^\infty\}_i = \hat{\delta}_\infty^i$ and $\{V^\infty\}_i = \hat{v}_\infty^i$.

The matrix K is called here *connectivity matrix* and contains information on how the blocks are connected together. Various geometrical configurations, such as those presented in Figure 2, can be described by adequately adjusting the components of the connectivity matrix.

Appendix B: Dynamic Simulations and SOC

We consider that the driver plate is moving under constant velocity, which is several orders of magnitude lower than the velocities of the blocks that are developed during abrupt sliding. Consequently, we can assume that the driver plate remains still during the sliding events. This situation is inspired by the far-field earth's tectonic movement, which is several orders of magnitudes lower (some centimeters per year) than the seismic slip velocities developed during earthquakes that can reach up to one meter per second.

For the simulations, we first calculate the minimum displacement of the driver plate that can trigger the sliding of at least one block. In this way, we avoid simulating the slow-dynamics (Stefanou, 2019), quasi-static behav-

ior of the system and we only integrate numerically the dynamic equations of motion of the system for determining its fast dynamics, unstable response. After each dynamic event, the system reaches a new equilibrium (local minimum potential energy state). The slip of the blocks is recorded and a random small overshoot in their displacements is considered (see also Brown et al., 1991; Rundle & Brown, 1991). The random overshoot is not the same between the blocks and varies from 0 to 20% of its slip during the previous event. The random overshoot embodies several uncertainties of the system related to its elastic parameters, initial conditions and frictional properties, among others.

The frictional properties of the blocks can be uniform or randomly chosen from a distribution. Slip or slip-rate softening is required to render the system unstable and lead to SOC behavior. Here, we use slip-weakening friction as in Huang et al. (1992); Stefanou (2019). Simulations with SRW would give similar results (cf. Carlson & Langer, 1989; Huang & Turcotte, 1992). In particular, the friction coefficient evolves from its static value (μ_s) to its kinetic one (μ_d). In the simulations presented here $\mu_s = 0.8$ and $\mu_d = 0.5$. The friction drop occurs in a dimensionless characteristic distance equal to $\hat{d}_c = 0.01$ (see also Section 2.3.1). The damping ratio ζ is set equal to 1 and $\frac{k_{ij}^c}{k_i^l} = 2$.

Each slip event can involve sliding of a single block, a cluster of some blocks or of all the blocks of the system. After each slip event the friction coefficient of each block is restored to its static friction value and a new period of quiescence takes place as shown in Figure 3.

The simulation procedure is summarized as follows:

1. *Quiescence period:* Determine $\hat{\delta}_\infty$ that renders the system unstable by solving $\Psi = 0$ and set the driver plate displacement equal to $\hat{\delta}_\infty = \min_{\forall i} \left(\left\{ \hat{\delta}_\infty \right\}_i \right)$
2. *Sudden slip event:* Integrate numerically the dynamic equations of motion Equation (A3) to determine slip $\hat{\delta}_i$, until $\max_{\forall i} (\hat{v}_i) \leq$ threshold. The threshold was set equal to 0.02, which is much smaller than the maximum velocity of blocks during unstable sliding (see Figures 3b–3d).
3. *Healing:* Set block velocities equal to zero and update their positions $\hat{\delta}_i^0 = \hat{\delta}_i + \tilde{\delta}_i$, where $\tilde{\delta}_i$ is a random overshoot as described above. Restore the friction of coefficient from μ_d to μ_s.

Repeat 1–3 and record events. A sequence of $N_0 = 10,000$ events were simulated for calculating the frequency-size statistics presented in Figure 4. The simulation of more events (20, 000) leads to almost identical results.

Appendix C: Numerical Implementation

The numerical integration of the ordinary differential equations presented herein was performed using *SciPy* (Virtanen et al., 2020) and the *LSODA* or *BDF* implicit algorithms (Hindmarsh, 1983; Petzold, 1983). The designed controller was programmed in *Python 3* (van Rossum, 1995) and the algebraic Riccati equation was solved using the *Python Control Systems Library* (Python Control Systems Library, 2020). The programs are available in *Jupyter notebooks* (Kluyver et al., 2016).

Data Availability Statement

The developed codes and the generated numerical data for all the examples presented in this study are publicly available in Zenodo repository in Stefanou and Tzortzopoulos (2022).

Acknowledgments
We would like to thank Pr. J.-P. Avouac, Dr A. Gualandi and Pr. S. Barbot for their feedback, constructive comments and fruitful discussions. This work was supported by the European Research Council (ERC) under the European Union Horizon 2020 research and innovation program (Grant agreement 757848 CoQuake), http://coquake.eu.

References

Abbott, S. (2015). *Understanding analysis*. Springer. Retrieved from https://books.google.gr/books?id=R2DkzQEACAAJ

Baisch, S., Koch, C., & Muntendam-Bos, A. (2019). Traffic light systems: To what extent can induced seismicity be controlled? *Seismological Research Letters*, *90*(3), 1145–1154. https://doi.org/10.1785/0220180337

Bak, P., & Chen, K. (1989). The physics of fractals. *Physica D: Nonlinear Phenomena*, *38*(1–3), 5–12. https://doi.org/10.1016/0167-2789(89)90166-8

Bak, P., Tang, C., & Wiesenfeld, K. (1988). Self-organized criticality. *Physical Review A*, *38*(1), 364–374. https://doi.org/10.1103/PhysRevA.38.364

Barbot, S. D. (2019). Slow-slip, slow earthquakes, period-two cycles, full and partial ruptures, and deterministic chaos in a single asperity fault. *Tectonophysics*, *768*, 228171. https://doi.org/10.1016/j.tecto.2019.228171

Barras, F., Aldam, M., Roch, T., Brener, E. A., Bouchbinder, E., & Molinari, J. F. (2019). Emergence of cracklike behavior of frictional rupture: The origin of stress drops. *Physical Review X*, *9*(4), 41043. https://doi.org/10.1103/PhysRevX.9.041043

Ben-Zion, Y. (2008). Collective behavior of earthquakes and faults. *Reviews of Geophysics*, *46*(4), 1–70. https://doi.org/10.1029/2008RG000260
Bhattacharya, P., & Viesca, R. C. (2019). Fluid-induced aseismic fault slip outpaces pore-fluid migration. *Science*, *364*(6439), 464–468. https://doi.org/10.1126/science.aaw7354
Birkeland, K. W., & Landry, C. C. (2002). Power-laws and snow avalanches. *Geophysical Research Letters*, *29*(11), 49–1–49–3. https://doi.org/10.1029/2001GL014623
Bommer, J. J., Crowley, H., & Pinho, R. (2015). A risk-mitigation approach to the management of induced seismicity. *Journal of Seismology*, *19*(2), 623–646. https://doi.org/10.1007/s10950-015-9478-z
Bommer, J. J., Oates, S., Cepeda, J. M., Lindholm, C., Bird, J., Torres, R., et al. (2006). Control of hazard due to seismicity induced by a hot fractured rock geothermal project. *Engineering Geology*, *83*(4), 287–306. https://doi.org/10.1016/j.enggeo.2005.11.002
Bosman, K., Baig, A., Viegas, G., & Urbancic, T. (2016). Towards an improved understanding of induced seismicity associated with hydraulic fracturing. *First Break*, *34*(7). https://doi.org/10.3997/1365-2397.34.7.86051
Boyd, J. P. (2000). *Chebyshev and fourier spectral methods* (2nd ed.). Dover Publications.
Brauer, F., & Nohel, J. (1969). *The qualitative theory of ordinary differential equations: An introduction*. Dover Publications.
Broccardo, M., Mignan, A., Grigoli, F., Karvounis, D., Pio Rinaldi, A., Danciu, L., et al. (2020). Induced seismicity risk analysis of the hydraulic stimulation of a geothermal well on Geldinganes, Iceland. *Natural Hazards and Earth System Sciences*, *20*(6), 1573–1593. https://doi.org/10.5194/nhess-20-1573-2020
Brown, S. R., Scholz, C. H., & Rundle, J. B. (1991). A simplified spring-block model of earthquakes. *Geophysical Research Letters*, *18*(2), 215–218. https://doi.org/10.1029/91GL00210
Brummitt, C. D., D'Souza, R. M., & Leicht, E. A. (2012). Suppressing cascades of load in interdependent networks. *Proceedings of the National Academy of Sciences*, *109*(12), E680–E689. https://doi.org/10.1073/pnas.1110586109
Burridge, R., & Knopoff, L. (1967). Model and theoretical seismicity. *Bulletin of the Seismological Society of America*, *57*(3), 341–371. https://doi.org/10.1785/bssa0570030341
Byerlee, J. D. (1978). Friction of rocks. *Pure and Applied Geophysics PAGEOPH*, *116*(4–5), 615–626. https://doi.org/10.1007/BF00876528
Cajueiro, D. O., & Andrade, R. F. (2010a). Controlling self-organized criticality in complex networks. *The European Physical Journal B*, *77*(2), 291–296. https://doi.org/10.1140/epjb/e2010-00229-8
Cajueiro, D. O., & Andrade, R. F. (2010b). Controlling self-organized criticality in sandpile models. *Physical Review E - Statistical, Nonlinear and Soft Matter Physics*, *81*(1), 1–10. https://doi.org/10.1103/PhysRevE.81.015102
Cajueiro, D. O., & Andrade, R. F. (2010c). Dynamical programming approach for controlling the directed Abelian Dhar-Ramaswamy model. *Physical Review E - Statistical, Nonlinear and Soft Matter Physics*, *82*(3), 1–12. https://doi.org/10.1103/PhysRevE.82.031108
Cappa, F., Scuderi, M. M., Collettini, C., Guglielmi, Y., & Avouac, J. P. (2019). Stabilization of fault slip by fluid injection in the laboratory and in situ. *Science Advances*, *5*(3), eaau4065. https://doi.org/10.1126/sciadv.aau4065
Carlson, J. M., & Langer, J. S. (1989). Mechanical model of an earthquake fault. *Physical Review A*, *40*(11), 6470–6484. https://doi.org/10.1103/PhysRevA.40.6470
Chester, F. M. (1994). Effects of temperature on friction: Constitutive equations and experiments with quartz gouge. *Journal of Geophysical Research*, *99*(B4), 7247. https://doi.org/10.1029/93JB03110
Chinnery, M. (1963). The stress changes that accompany strike-slip faulting. *Bulletin of the Seismological Society of America*, *53*(5), 921–932. https://doi.org/10.1785/bssa0530050921
Collins-Craft, N. A., Stefanou, I., Sulem, J., & Einav, I. (2020). A Cosserat Breakage Mechanics model for brittle granular media. *Journal of the Mechanics and Physics of Solids*, *141*(0), 103975. https://doi.org/10.1016/j.jmps.2020.103975
Cornet, F. H. (2016). Seismic and aseismic motions generated by fluid injections. *Geomechanics for Energy and the Environment*, *5*, 42–54. https://doi.org/10.1016/j.gete.2015.12.003
Dhar, D., & Ramaswamy, R. (1989). Exactly solved model of self-organized critical phenomena. *Physical Review Letters*, *63*(16), 1659–1662. https://doi.org/10.1103/PhysRevLett.63.1659
Dieterich, J. H. (1972). Time-dependent friction as a possible mechanism for aftershocks. *Journal of Geophysical Research*, *77*(20), 3771–3781. https://doi.org/10.1029/JB077i020p03771
Dieterich, J. H. (1979). Modeling of rock friction: 1. Experimental results and constitutive equations. *Journal of Geophysical Research*, *84*(B5), 2161. https://doi.org/10.1029/JB084iB05p02161
Dieterich, J. H. (1981). Constitutive properties of faults with simulated gouge. *Mechanical behavior of crustal rocks*, *24*, 103–120. https://doi.org/10.1029/GM024p0103
Erickson, B. A., Birnir, B., & Lavallée, D. (2011). Periodicity, chaos and localization in a Burridge-Knopoff model of an earthquake with rate-and-state friction. *Geophysical Journal International*, *187*(1), 178–198. https://doi.org/10.1111/j.1365-246X.2011.05123.x
Erickson, B. A., Jiang, J., Barall, M., Lapusta, N., Dunham, E. M., Harris, R., et al. (2020). The community code verification exercise for simulating sequences of earthquakes and aseismic slip (SEAS). *Seismological Research Letters*, *91*(2A), 874–890. https://doi.org/10.1785/0220190248
Frash, L. P., Fu, P., Morris, J., Gutierrez, M., Neupane, G., Hampton, J., et al. (2021). Fracture caging to limit induced seismicity. *Geophysical Research Letters*, *48*(1), e2020GL090648. https://doi.org/10.1029/2020GL090648
Fung, Y. C. (1965). *Foundations of solid mechanics*. Prentice Hall.
Gualandi, A., Avouac, J., Michel, S., & Faranda, D. (2020). *The predictable chaos of slow earthquakes* (Vol. 6). Science Advances. Accepted. https://doi.org/10.1126/sciadv.aaz5548
Guglielmi, Y., Cappa, F., Avouac, J., Henry, P., & Elsworth, D. (2015). Seismicity triggered by fluid injection-induced aseismic slip. *Science*, *348*(6240), 1224–1226. https://doi.org/10.1126/science.aab0476
Gutiérrez-Oribio, D., Tzortzopoulos, G., Stefanou, I., & Plestan, F. (2022). *Earthquake control: An emerging application for robust control. theory and experimental tests*. https://doi.org/10.48550/ARXIV.2203.00296
Häring, M. O., Schanz, U., Ladner, F., & Dyer, B. C. (2008). Characterisation of the Basel 1 enhanced geothermal system. *Geothermics*, *37*(5), 469–495. https://doi.org/10.1016/j.geothermics.2008.06.002
Hindmarsh, A. C. (1983). *ODEPACK, A systematized collection of ODE solvers*. In R. S. Stepleman & E. Al (Eds.) *Imacs transactions on scientific computation*, (Vol. 1, pp. 55–64). Amstredam.
Hoffmann, H., & Payton, D. W. (2014). Suppressing cascades in a self-organized-critical model with non-contiguous spread of failures. *Chaos, Solitons & Fractals*, *67*, 87–93. https://doi.org/10.1016/j.chaos.2014.06.011
Hofmann, H., Zimmermann, G., Farkas, M., Huenges, E., Zang, A., Leonhardt, M., et al. (2019). First field application of cyclic soft stimulation at the Pohang Enhanced Geothermal System site in Korea. *Geophysical Journal International*, *217*(2), 926–949. https://doi.org/10.1093/gji/ggz058

Hofmann, H., Zimmermann, G., Zang, A., & Min, K. B. (2018). Cyclic soft stimulation (CSS): A new fluid injection protocol and traffic light system to mitigate seismic risks of hydraulic stimulation treatments. *Geothermal Energy*, *6*(1), 27. https://doi.org/10.1186/s40517-018-0114-3

Huang, J., Narkounskaia, G., & Turcotte, D. L. (1992). A cellular-automata, slider-block model for earthquakes II. Demonstration of self-organized criticality for a 2-D system. *Geophysical Journal International*, *111*(2), 259–269. https://doi.org/10.1111/j.1365-246X.1992.tb00575.x

Huang, J., & Turcotte, D. L. (1992). Chaotic seismic faulting with a mass-spring model and velocity-weakening friction. *Pure and Applied Geophysics PAGEOPH*, *138*(4), 569–589. https://doi.org/10.1007/BF00876339

Ito, K., & Matsuzaki, M. (1990). Earthquakes as self-organized critical phenomena. *Journal of Geophysical Research*, *95*(B5), 6853. https://doi.org/10.1029/JB095iB05p06853

Kanamori, H., & Brodsky, E. E. (2004). The physics of earthquakes. *Reports on Progress in Physics*, *67*(8), 1429–1496. https://doi.org/10.1088/0034-4885/67/8/R03

Kenigsberg, A. R., Rivière, J., Marone, C., & Saffer, D. M. (2020). Evolution of elastic and mechanical properties during fault shear: The roles of clay content, fabric development, and porosity. *Journal of Geophysical Research: Solid Earth*, *125*(3), 1–16. https://doi.org/10.1029/2019JB018612

Keranen, K. M., Savage, H. M., Abers, G. A., & Cochran, E. S. (2013). Potentially induced earthquakes in Oklahoma, USA: Links between wastewater injection and the 2011 Mw 5.7 earthquake sequence. *Geology*, *41*(6), 699–702. https://doi.org/10.1130/G34045.1

Khalil, H. k. (2015). *Non-linear control* (Global edition). Pearson.

Kluyver, T., Ragan-Kelley, B., Pérez, F., Granger, B., Bussonnier, M., Frederic, J., et al. (2016). Jupyter Notebooks – A publishing format for reproducible computational workflows. In F. Loizides & B. Schmidt (Eds.), *Positioning and power in academic publishing: Players, agents and agendas* (pp. 87–90).

Kwiatek, G., Saarno, T., Ader, T., Bluemle, F., Bohnhoff, M., Chendorain, M., et al. (2019). Controlling fluid-induced seismicity during a 6.1-km-deep geothermal stimulation in Finland. *Science Advances*, *5*(5), eaav7224. https://doi.org/10.1126/sciadv.aav7224

Lachenbruch, A. H. (1980). Frictional heating, fluid pressure, and the resistance to fault motion. *Journal of Geophysical Research*, *85*(B11), 6097–6112. https://doi.org/10.1029/JB085iB11p06097

Larochelle, S., Lapusta, N., Ampuero, J.-P., & Cappa, F. (2021). Constraining fault friction and stability with fluid-injection field experiments. *Geophysical Research Letters*, *48*(10), 1–17. https://doi.org/10.1029/2020GL091188

Lewis, F., Vrabie, D., & Syrmos, V. (2012). *Optimal control*. Wiley. https://doi.org/10.1002/9781118122631

Lyapunov, A. M. (1966). *Stability of motion*. Academic Press.

McClung, D., & Schaerer, P. (1993). *The avalanche handbook*. The mountainers.

McGarr, A., Simpson, D., & Seeber, L. (2002). Case histories of induced and triggered seismicity. *International Handbook of Earthquake and Engineering Seismology*, *81*(A), 0–12.

Narkounskaia, G., Huang, J., & Turcotte, D. L. (1992). Chaotic and self-organized critical behavior of a generalized slider-block model. *Journal of Statistical Physics*, *67*(5–6), 1151–1183. https://doi.org/10.1007/BF01049013

Noël, P. A., Brummitt, C. D., & D'Souza, R. M. (2013). Controlling self-organizing dynamics on networks using models that self-organize. *Physical Review Letters*, *111*(7), 1–5. https://doi.org/10.1103/PhysRevLett.111.078701

Papachristos, E., & Stefanou, I. (2021). *Artificial Intelligence in the service of earthquake prevention*. to be submitted.

Petzold, L. (1983). Automatic selection of methods for solving stiff and nonstiff systems of ordinary differential equations. *SIAM Journal on Scientific and Statistical Computing*, *4*(1), 136–148. https://doi.org/10.1137/0904010

Pipping, E. (2019). Existence of long-time solutions to dynamic problems of viscoelasticity with rate-and-state friction. *ZAMM Zeitschrift fur Angewandte Mathematik und Mechanik*, *99*(11), 1–10. https://doi.org/10.1002/zamm.201800263

Python Control Systems Library. (2020). Retrieved from https://python-control.readthedocs.io/en/0.8.3/

Raleigh, C. B., Healy, J. H., & Bredehoeft, J. D. (1976). An experiment in earthquake control at Rangely, Colorado. *Science*, *191*(4233), 1230–1237. https://doi.org/10.1126/science.191.4233.1230

Rattez, H., Stefanou, I., & Sulem, J. (2018). The importance of Thermo-Hydro-Mechanical couplings and microstructure to strain localization in 3D continua with application to seismic faults. Part I: Theory and linear stability analysis. *Journal of the Mechanics and Physics of Solids*, *115*, 54–76. https://doi.org/10.1016/j.jmps.2018.03.004

Rattez, H., Stefanou, I., Sulem, J., Veveakis, M., & Poulet, T. (2018). The importance of Thermo-Hydro-Mechanical couplings and microstructure to strain localization in 3D continua with application to seismic faults. Part II: Numerical implementation and post-bifurcation analysis. *Journal of the Mechanics and Physics of Solids*, *115*, 1–29. https://doi.org/10.1016/j.jmps.2018.03.003

Rattez, H., & Veveakis, M. (2020). Weak phases production and heat generation control fault friction during seismic slip. *Nature Communications*, *11*(1), 1–8. https://doi.org/10.1038/s41467-019-14252-5

Rice, J. R. (1993). Spatio-temporal complexity of slip on a fault. *Journal of Geophysical Research*, *98*(B6), 9885. https://doi.org/10.1029/93JB00191

Rice, J. R. (2006). Heating and weakening of faults during earthquake slip. *Journal of Geophysical Research*, *111*(B5), B05311. https://doi.org/10.1029/2005JB004006

Rubinstein, J. L., & Mahani, A. B. (2015). Myths and facts on wastewater injection, hydraulic fracturing, enhanced oil recovery, and induced seismicity. *Seismological Research Letters*, *86*(4), 1060–1067. https://doi.org/10.1785/0220150067

Rudnicki, J. W., & Chen, C. H. (1988). Stabilization of rapid frictional slip on a weakening fault by dilatant hardening. *Journal of Geophysical Research*, *93*(B5), 4745–4757. https://doi.org/10.1029/JB093iB05p04745

Ruina, A. (1983). Slip instability and state variable friction laws. *Journal of Geophysical Research*, *88*(B12), 10359–10370. https://doi.org/10.1029/JB088iB12p10359

Rundle, J. B., & Brown, S. R. (1991). Origin of rate dependence in frictional sliding. *Journal of Statistical Physics*, *65*(1–2), 403–412. https://doi.org/10.1007/BF01329869

Scholz, C. H. (2019). *The mechanics of earthquakes and faulting* (3rd ed.). Cambridge University Press. https://doi.org/10.1017/9781316681473

Scuderi, M. M., & Collettini, C. (2018). Fluid injection and the mechanics of frictional stability of shale-bearing faults. *Journal of Geophysical Research: Solid Earth*, *123*(10), 8364–8384. https://doi.org/10.1029/2018JB016084

Sornette, D. (1999). Earthquake debate - didier sornette. *Nature*. https://doi.org/10.1038/nature28132

Stathas, A., & Stefanou, I. (2022). *Fault friction under thermal pressurization during large coseismic-slip part i: Numerical analyses*. arXiv. https://doi.org/10.48550/ARXIV.2205.00314

Stefanou, I. (2019). Controlling anthropogenic and natural seismicity: Insights from active stabilization of the spring-slider model. *Journal of Geophysical Research: Solid Earth*, *124*(8), 8786–8802. https://doi.org/10.1029/2019JB017847

Stefanou, I., & Alevizos, S. (2016). Fundamentals of bifurcation theory and stability analysis. In J. Sulem, I. Stefanou, E. Papamichos, & E. Veveakis (Eds.), *Modelling of instabilities and bifurcation in geomechanics, alert geomaterials doctoral school 2016. Aussois, France*. Retrieved from https://www.researchgate.net/publication/334164186

Stefanou, I., & Tzortzopoulos, G. (2022). *Preventing instabilities and inducing controlled, slow-slip in frictionally unstable systems: Developed Codes + Numerical Data*. https://doi.org/10.5281/zenodo.6552972

Terzaghi, K. (1925). *Erdbaumechanik auf bodenphysikalischer grundlage*. Wien: F. Deuticke.

Tinti, E., Scuderi, M. M., Scognamiglio, L., Di Stefano, G., Marone, C., & Collettini, C. (2016). On the evolution of elastic properties during laboratory stick-slip experiments spanning the transition from slow slip to dynamic rupture. *Journal of Geophysical Research: Solid Earth*, *121*(12), 8569–8594. https://doi.org/10.1002/2016JB013545

Turcotte, D. L. (1999). Self-organized criticality. *Reports on Progress in Physics*, *62*(10), 1377–1429. https://doi.org/10.1088/0034-4885/62/10/201

Tzortzopoulos, G. (2021a). *Controlling earthquakes (coquake) in the laboratory using pertinent fault stimulating techniques (Unpublished doctoral dissertation)*. Ecole Centrale de Nantes.

Tzortzopoulos, G. (2021b). *Phd thesis defense presentation of mr. georgios tzortzopoulos. Youtube*. Retrieved from https://youtu.be/xyvAtueAmRU

Tzortzopoulos, G., Braun, P., & Stefanou, I. (2021). Absorbent porous paper reveals how earthquakes could be mitigated. *Geophysical Research Letters*, *48*(3). https://doi.org/10.1029/2020GL090792

van Rossum, G. (1995). *Python tutorial. CWI Report CS-R9526, CS-R9526, 1–65*. Retrieved from http://oai.cwi.nl/oai/asset/5007/05007D.pdf

Vardoulakis, I. (2000). Catastrophic landslides due to frictional heating of the failure plane. *Mechanics of Cohesive-Frictional Materials*, *5*(6), 443–467. https://doi.org/10.1002/1099-1484(200008)5:6<443::AID-CFM104>3.0.CO;2-W

Vardulakis, A. I. (1991). *Linear multivariable control: Algebraic analysis and synthesis control*. John Wiley & Sons, Inc.

Vardulakis, A. I. (2012). *Introduction to the mathematical theory of the theory of signals, systems and control*. Tziola.

Verdon, J. P., & Bommer, J. J. (2021). Green, yellow, red, or out of the blue? An assessment of traffic light schemes to mitigate the impact of hydraulic fracturing-induced seismicity. *Journal of Seismology*, *25*(1), 301–326. https://doi.org/10.1007/s10950-020-09966-9

Virtanen, P., Gommers, R., Oliphant, T. E., Haberland, M., Reddy, T., Cournapeau, D., et al. (2020). SciPy 1.0: Fundamental algorithms for scientific computing in Python. *Nature Methods*, *17*(3), 261–272. https://doi.org/10.1038/s41592-019-0686-2

Walters, R. J., Zoback, M. D., Baker, J. W., & Beroza, G. C. (2015). Characterizing and responding to seismic risk associated with earthquakes potentially triggered by fluid disposal and hydraulic fracturing. *Seismological Research Letters*, *86*(4), 1110–1118. https://doi.org/10.1785/0220150048

Watkins, N. W., Pruessner, G., Chapman, S. C., Crosby, N. B., & Jensen, H. J. (2016). 25 Years of self-organized criticality: Concepts and controversies. *Space Science Reviews*, *198*(1–4), 3–44. https://doi.org/10.1007/s11214-015-0155-x

Wolfram, S. (1983). Statistical mechanics of cellular automata. *Reviews of Modern Physics*, *55*(3), 601–644. https://doi.org/10.1103/RevModPhys.55.601

Zang, A., Zimmermann, G., Hofmann, H., Stephansson, O., Min, K. B., & Kim, K. Y. (2019). How to reduce fluid-injection-induced seismicity. *Rock Mechanics and Rock Engineering*, *52*(2), 475–493. https://doi.org/10.1007/s00603-018-1467-4

Zhou, K., Doyle, J., & Glover, K. (1996). *Robust and optimal control*. Prentice Hall.